A Joint Seismic and Space-Based Investigation of the 2016 Lamplugh Glacier and 2017 Wrangell Mountains (Alaska) Landslides

Xinyu Luo[1], Wenyuan Fan[1] [ID], and Yuri Fialko[1] [ID]

[1]Scripps Institution of Oceanography, University of California, San Diego, La Jolla, California, USA

Abstract Landslides commonly occur in areas with steep topography and abundant precipitation and pose a significant hazard to local communities. Some of the largest known landslides occur in Alaska, including several that caused local tsunamis. Many landslides may have gone undetected in remote areas due to lack of observations. Here, we develop a semiautomated workflow using both seismic and geodetic observations to detect, locate, validate, and characterize landslides in Alaska. Seismic observations have shown promise in continuously monitoring landslide occurrence, while remote sensing techniques are well suited for verification and high-resolution imaging of landslides. We validate our procedure using the 28 June 2016, Lamplugh Glacier landslide. We also present observations of a previously unknown landslide occurred on 22 September 2017 in the Wrangell Mountains region. The Wrangell Mountains landslide generated a coherent surface wavefield recorded across Alaska and the contiguous United States. We used Sentinel-1 Synthetic Aperture Radar and Sentinel-2 optical imagery to map the respective mass deposit. To investigate the landslide dynamics, we inverted regional seismic surface wave data for a centroid single force failure model. Our model suggests that the Wrangell Mountains landslide lasted for about 140 s and had two subevents involving at least five distinct stages. We estimate that the landslide had displaced 3.1–13.4 million tons of rocks over a distance of ~2 km. Our results suggest that combining seismic and geodetic observations can vastly improve the detection and characterization of landslides in remote areas in Alaska and elsewhere, providing new insights into the landslide dynamics.

Plain Language Summary Landslides are mass wasting events that can involve a variety of processes such as rock falls, avalanches, debris flows, slumping, and creep, all of which ultimately result in displacement of large volumes of Earth materials downslope due to gravity. Rapidly moving landslides are some of the most devastating natural disasters. Much of data on landslides come from events that affect populated areas; however, many more landslides are expected to occur in remote areas and go unnoticed. In this study, we develop a procedure that systematically combines seismic and space-based observations to detect and investigate remote landslides in Alaska. We identified a previously unknown landslide that occurred on 22 September 2017 in the Wrangell Mountains region. This event displaced millions of tons of shallow Earth materials in a matter of minutes. Our method can be used to systematically investigate landslides in Alaska, as well as other remote regions around the globe.

1. Introduction

Landslides can denude mountains, transport sediments to fluvial networks, and impact regional ecosystems by drastically changing the landscape (e.g., Benda & Dunne, 1997; Gomi et al., 2002; Imaizumi & Sidle, 2007; Korup, 2005). Landslides involve hydromechanical processes that move rocks and sediments downhill, driven by gravitational forces (e.g., X. Fan et al., 2017; Gomberg et al., 1995; Milillo et al., 2014). A broad range of mass wasting events can be categorized as landslides, such as debris flows, lahars, slope creep, and avalanches (e.g., Allstadt, 2013; Delbridge et al., 2016; Iverson et al., 2000; Lai et al., 2018). Such events can last from minutes to years (e.g., Ekström & Stark, 2013; Gualtieri & Ekström, 2018; Hu et al., 2019) and result in significant damage and casualties (Froude & Petley, 2018; Hibert et al., 2015; Petley, 2012). In addition to mass wasting, landslides that occur near bodies of water may produce local tsunamis and further endanger local communities (Bardet et al., 2003; Dufresne et al., 2018). Despite much progress made toward understanding of landslides and the associated hazards, a number of questions remain, largely due to a lack of systematic characterization of the
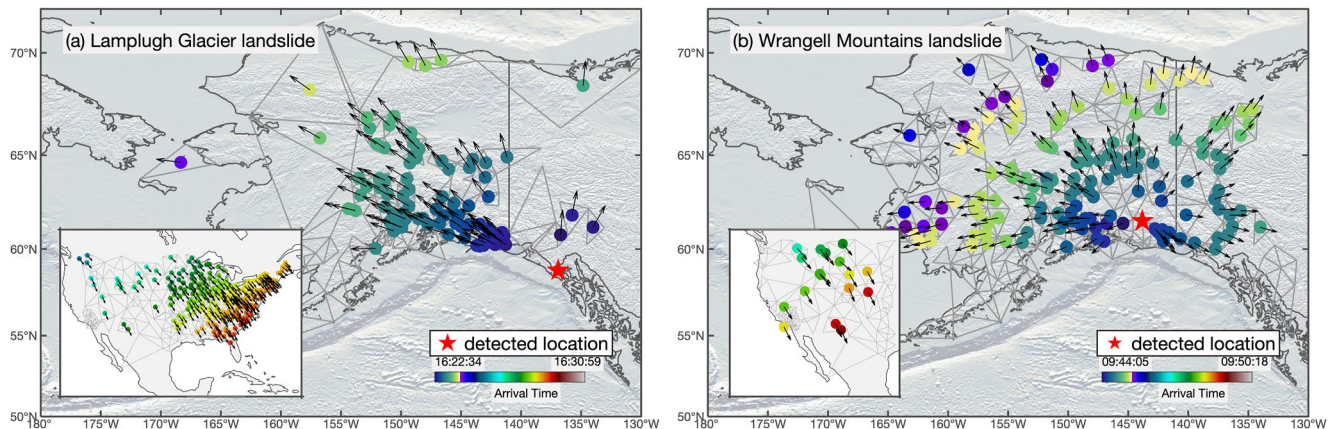
Figure 1. Rayleigh wavefields of the 28 June, 2016, Lamplugh Glacier landslide (a) and the 22 September, 2017 Wrangell Mountains landslide (b). Surface wave propagation directions and arrival times are shown as the arrows and dots, respectively. Triad subarrays are shown as gray triangles. Red stars are the seismically resolved locations. Insets show wavefields in the contiguous United States.

principal physical parameters of landslides such as their location, time, volume, and sliding speed (Ekström & Stark, 2013; Mondini et al., 2021).

It is challenging to continuously monitor landslides in remote regions because conventional methods such as field and aerial surveys are costly and time-consuming, and typically limited to case studies (Dufresne et al., 2019; Guthrie et al., 2012; Toney et al., 2021). Due to the challenging terrain conditions, field investigations of Alaska landslides are infrequent and have been mainly conducted in coastal regions (Hibert et al., 2015). For this reason, relatively few landslides have been reported in Alaska (Bahavar et al., 2019; Kirschbaum et al., 2015), despite the fact that they include some of the largest landslides observed in the United States. For example, the 2015 Taan Fjord landslide near Icy Bay mobilized 180 million tons of rocks and produced a local tsunami reaching as high as 193 m (Higman et al., 2018). As slope failure occurrence correlates with the topographic relief in mountainous areas (Korup et al., 2007), landslides likely occur frequently in Alaska but undetected (Kirschbaum et al., 2015).

Remote sensing methods, such as Synthetic Aperture Radar (SAR), have been increasingly exploited to study landslides (Colesanti & Wasowski, 2006; Fruneau et al., 1996; Singhroy et al., 1998). For example, SAR can directly image the surface disturbance due to landslides at a high spatial resolution by comparing the image amplitude changes or phase coherence between radar acquisitions taken before and after an event (e.g., Mondini et al., 2021). Additionally, satellite or aerial optical imagery can provide ground-truth observations to determine exact landslide location, composition, area, and runoff distance (Dufresne et al., 2019; Lacroix et al., 2018; Qu et al., 2021). However, due to infrequent acquisitions, exact timing of landslides and details of their initiation cannot be solely resolved using space-based observations (Mondini et al., 2021). Additionally, weather may thwart optical satellite observations, further reducing usable images.

Seismic observations have shown promise in identifying landslides (Ekström, 2006; W. Fan et al., 2020; Manconi et al., 2016; Xie et al., 2020) and resolving landslide dynamics (Brodsky et al., 2003; Intrieri et al., 2018; Kanamori & Given, 1982; Lai et al., 2018; Poli, 2017). Fast-moving landslides can generate seismic signals from short-period (≥ 1 Hz; Doi & Maeda, 2020; Hibert et al., 2011; Yamada et al., 2012) to intermediate and long-period motion (≤ 0.1 Hz; Allstadt, 2013; Kanamori & Given, 1982; Eissler & Kanamori, 1987). Particularly, the intermediate- to long-period (20–150 s) seismic waves can often be observed globally and have been used to study landslide occurrence in remote regions (Ekström, 2006; Ekström & Stark, 2013; W. Fan et al., 2018). The seismic records have a high temporal resolution and may be used to continuously monitor landslides, complementing the space-based observations (e.g., W. Fan et al., 2018; Okuwaki et al., 2021).

Here, we develop a semiautomated workflow combining space-based and seismic observations to detect and locate Alaska landslides and further use the suite of geophysical observations to infer landslide failure processes. We first apply the method to the well-documented 2016 Lamplugh Glacier landslide (Bessette-Kirton et al., 2018; Coe et al., 2018; Dufresne et al., 2019) to verify our procedure. We then use our method to identify a previously unknown landslide that occurred on 22 September 2017 in the Wrangell Mountains region in Alaska (Figure 1).

As we demonstrate below, the 2017 Wrangell Mountain landslide had two subevents and a multiple-stage failure process. The results demonstrate the effectiveness of the procedure and offer new insights into the failure dynamics of complex landslides in Alaska.

2. Data

2.1. Seismic Data

We use continuous, vertical-component, broadband seismic data to locate landslides with stations registered at the International Federation of Digital Seismograph Networks (FDSN) (see Data Availability Statement for details). The data were downloaded from the Data Management Center (DMC) of the Incorporated Research Institution for Seismology (IRIS). The original records are sampled at 1 Hz, and we band-pass filter them in the 20–50 s period band using a fourth-order Butterworth filter.

To investigate the landslide failure dynamics, near-field to regional-distance seismic records are used for inverting centroid single force (CSF) models of the landslides (Figures 2–6). We use three-component, broadband displacement records from stations within five degrees of the landslide location to invert for the CSF models (see Open Research for details). The records are sampled at 40 or 50 Hz, and we fit waveforms in a 200 s long time window around the surface waves: assuming an apparent move out velocity of 3.7 km/s, the time window is selected as 40 s before and 160 s after the predicted arrival time, and the waveforms are tapered before being used for the CSF inversion. Additionally, we inspect high-frequency (1–10 Hz) radiation of near-field stations (Figure 2) to confirm the nature of the seismic sources.

2.2. Space Geodetic and Remote Sensing Data

We use Sentinel-2 optical imagery to confirm whether the seismically detected sources are indeed associated with landslides (Figure 8). The optical images are downloaded from Copernicus Open Access Hub of the European Space Agency. We use images from bands 2, 3, and 4 of the Multispectral Instrument on board of the Sentinel-2A and Sentinel-2B satellites to generate a true color composite of the regions of interest. In addition to the optical imagery, we use SAR data from the Sentinel-1A satellite (Figures 7 and 9). The SAR data offer independent confirmation and validation of the events and are highly complementary to the Sentinel-2 optical imagery. The data were processed using GMTSAR (Jin & Fialko, 2020; Sandwell et al., 2011; Tymofyeyeva et al., 2019). We calculate the radar amplitude for each acquisition date and coherence of the interferometric phase. Both the phase coherence and variations in the radar amplitude can carry information about surface changes caused by landslides.

3. Methods

3.1. Detecting Hidden Seismic Sources Using Coherent Seismic Surface Wavefields

We use AELUMA (Automated Event Location Using a Mesh of Arrays) to detect and locate seismic sources in Alaska (de Groot-Hedlin & Hedlin, 2015; W. Fan et al., 2018). The method uses surface waves recorded by large aperture arrays to identify seismic sources. It first detects coherent surface wave signals using subarrays and then assembles the measured surface wave arrival angles to locate the seismic sources, assuming that the waves propagate along great circle paths (W. Fan et al., 2018). In practice, we first divide the large arrays into nonoverlapping three-station subarrays (triads). Each triad is required to have internal angles between 30 and 120° to reliably resolve the arrival angles. Next, beamforming analysis is applied to band-passed filtered (20–50 s) continuous data to detect coherent signals. We use a 600 s long sliding time window and a 300 s increment step to examine the data. The beamforming analysis is applied to each triad and time window independently. The detections are screened through a quality control procedure, such as examining the average cross-correlation coefficient, local phase velocity, and beam-power value of each detection (W. Fan et al., 2018). The remaining detections are used for association, which are grouped into nonoverlapping clusters. Each cluster is then used to locate one seismic source, and its location uncertainty is empirically estimated by examining the spatial structure of candidate source locations that yield misfits within a predefined threshold (de Groot-Hedlin & Hedlin, 2018; W. Fan et al., 2018, 2020). Finally, the quality of each located seismic event is assessed to avoid duplicates and a catalog is populated. The approach is data-driven, makes few assumptions about the nature of the seismic sources,
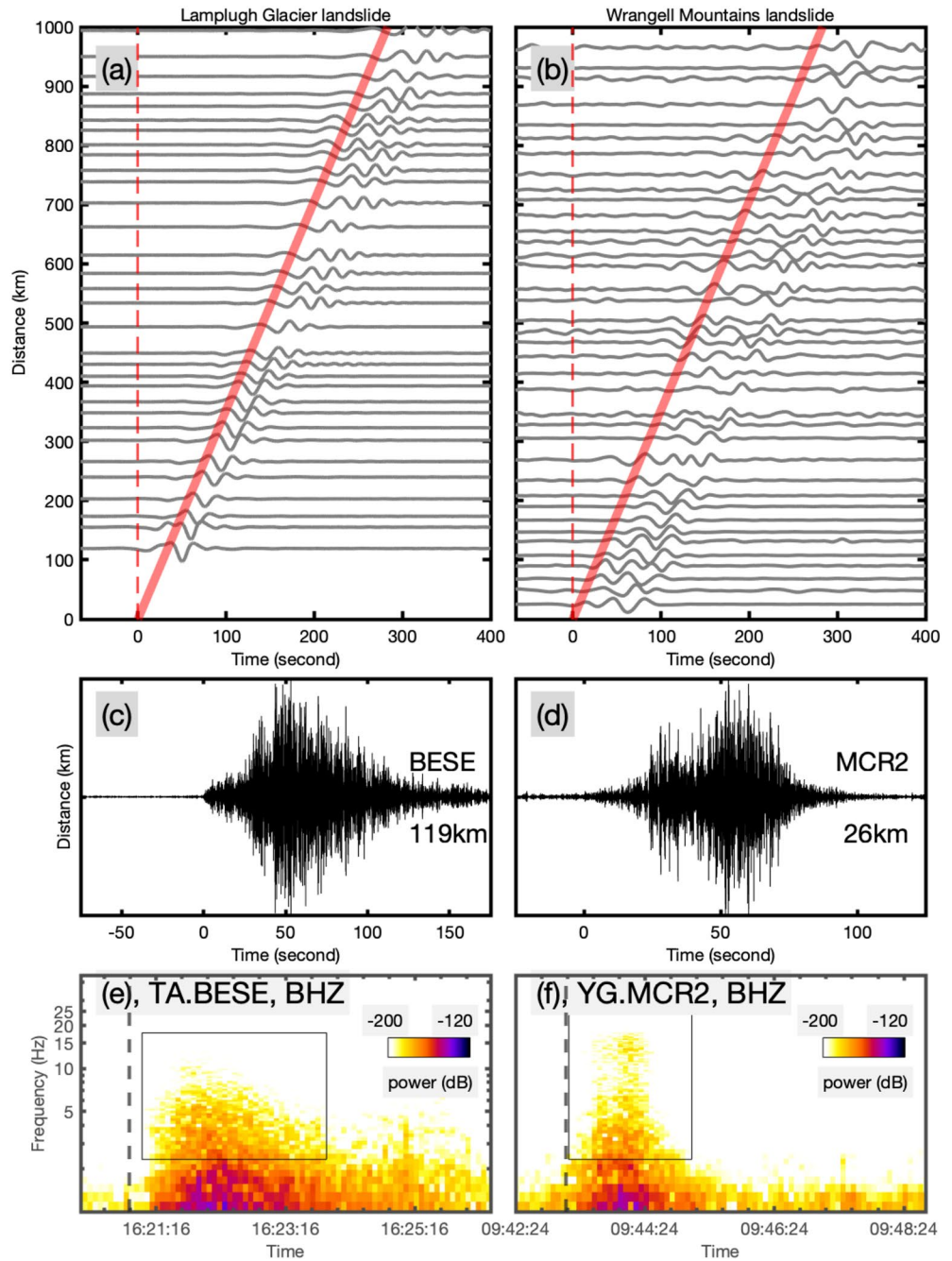
Figure 2. Record sections that are aligned using the seismically resolved locations in Figure 1. Records are normalized by their peak amplitudes, respectively, and they are band-pass filtered to show signals in the 20–70 s period band. Red lines show a 3.6 km/s reference move out velocity. AELUMA origin time (0 s) denotes 16:20:53 (UTC) for the Lamplugh Glacier landslide and 09:43:11 (UTC) for the Wrangell Mountains landslide. (a) Vertical record section of the 28 June, 2016, Lamplugh Glacier landslide. (b) Vertical record section of the 22 September, 2017 Wrangell Mountain landslide. (c) Vertical high-frequency record (0.1–1 s period) of the 2016 Lamplugh Glacier landslide at the nearest station BESE (119 km away). (d) Vertical high-frequency record (0.1–1 s period) of the 2017 Wrangell Mountain landslide at the nearest station MCR2 (26 km away). High-frequency records have spindle shapes for both events. Spectrograms of vertical component at BESE (e) for the 2016 Lamplugh Glacier landslide and at MCR2 (f) for the 2017 Wrangell Mountain landslide. Gray boxes show the part where the stations have recorded high frequency (>1 Hz) radiation.
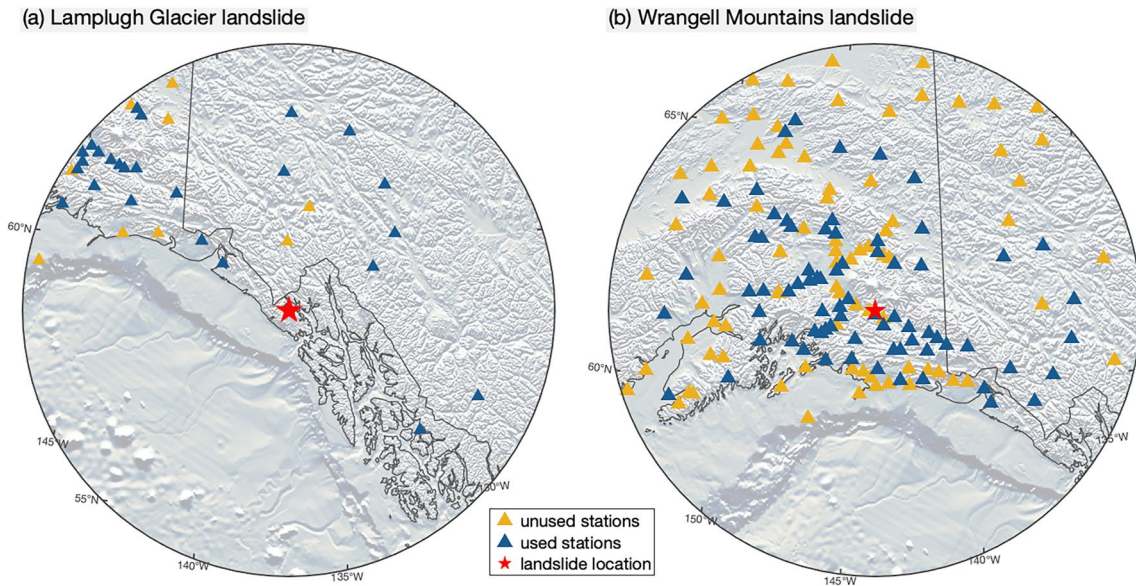
Figure 3. Stations used for centroid single force (CSF) inversions. (a) Lamplugh Glacier landslide. (b) Wrangell Mountains landslide. Red stars show seismic locations of landslides. Maps show stations within five degrees of the landslides. Blue triangles indicate the stations used in the CSF inversion. Yellow triangles indicate the stations that are within the five-degree searching range but are not selected for inversions.

and does not need a velocity model (W. Fan et al., 2018). The method is particularly well-suited for detecting unconventional seismic sources such as landslides that are commonly missed in standard catalogs (W. Fan et al., 2019, 2020; Okuwaki et al., 2021). However, the method does not resolve the driving physical processes of the detected seismic sources, for example, earthquakes or landslides. Therefore, we further use space-based observations to confirm and validate the nature of the detected sources (Section 3.3) and apply seismic waveform inversion to resolve the source mechanisms (Section 3.2) below.

3.2. Centroid Single Force Inversion

The acceleration and deceleration of a landslide moving downhill is expected to impose shear tractions at the sliding interface, which can be approximated as centroid single forces (CSF; Kanamori & Given, 1982; Kawakatsu, 1989). The sliding process can generate broadband seismic surface waves propagating up to thousands of kilometers if the landslide is sufficiently large, couples well with solid Earth, does not significantly disintegrate, and moves rapidly (Allstadt, 2013; Fukao, 1995). The CSF models can offer high-resolution insights into the landslide failure process and characteristics (e.g., Allstadt, 2013). Here, we use regional three-component broadband seismic records to invert for CSF models of the 2016 Lamplugh Glacier and 2017 Wrangell Mountains landslides (Figures 3–5). We use a frequency-domain inversion method derived from W. Fan et al. (2014), which was initially designed for finite-fault slip inversion. We apply the inversion scheme iteratively to update the model by gradually including usable traces within five degrees of the landslides.

The landslide displacement waveforms are convolutions between the CSF model and the Green's functions for a given source-receiver pair. In the frequency domain, the displacement spectra are linearly related to the CSF spectra (Equation 1), which can be inverted for each frequency bin independently. In a discrete format, the linear relation can be written as follows:

$$u_n(\underline{x}, \omega) = G_{ni}(\underline{x}, \omega) F_i(\omega), \tag{1}$$

where u_n, G_{ni}, and F_i are the spectra of the displacement seismogram, Green's function, and CSF; ω is the angular frequency; x denotes the relative locations between the source and receiver; and n and i are the receiver- and source-side directions, respectively. The failure history of a CSF model is then obtained from the inverse Fourier transform of its estimated spectra. The zero-frequency spectra are set as zero to ensure that the net forces are zero. We minimize ℓ_1 data misfit in the inversion (Equation 2) to obtain robust models, different from the ℓ_2

minimization used in conventional methods, and the procedure is effective when using a large number of stations with observation outliers:

$$\mathbf{F} = \arg\min \|\mathbf{u} - \mathbf{G} \cdot \mathbf{F}\|_1. \tag{2}$$

In this study, we use the ground-truth locations obtained from the remote-sensing observations (Table S1 in Supporting Information S1) to compute the Green's functions at each station for the CSF inversion. The remote sensing locations are defined as the mountain piedmonts. The Green's function is obtained using the Instaseis method (van Driel et al., 2015), which extracts Green's functions from a precomputed database that is computed using the axisymmetric spectral-element method (Nissen-Meyer et al., 2014). The ℓ_1 inverse problem is solved using convex optimization (CVX package; Grant & Boyd, 2008, 2014).

In practice, the seismic data are first detrended and the instrument response is removed. We invert CSF spectra in the 20–70 s period band (0.014–0.02 Hz) after applying a Tukey taper with a cosine fraction of 15% to the 200 s long records. The period band is different from the surface wave period band (20–50 s) used for detecting seismic sources with the AELUMA procedure. The 20–50 s period band is ideal for surface wave detection and location because of its low noise level. For the CSF inversion, we aim to include as much low-frequency signals as data permits, hoping to resolve a more complete failure process (Ekström & Stark, 2013). The 20–70 s period band is empirically selected to maximize the useable frequency content from the data (e.g., Ekström & Stark, 2013). We gradually include all usable data and iteratively update the CSF model. We first manually select a set of seismic traces to obtain an initial model, and traces are selected to have clear event signals and low background noise. With the initial model, we forward compute synthetic waveforms at all stations for all three components. The synthetic waveforms ($\mathbf{u}^s$) are cross-correlated with the observations, and the normalized residual is computed for each trace. Here the normalized residual is defined as $\|\mathbf{u} - \mathbf{u}^s\|_1/\|\mathbf{u}\|_1$ using the ℓ_1 misfit. Traces with cross-correlation (CC) coefficients above a threshold of 0.6 and normalized residual below a threshold of 0.7 are included to invert for a new CSF model. The cross-correlation procedure emphasizes waveform similarity, and it offers a different measure of the CSF model quality from the waveform misfit. Such an inversion-update procedure is repeated until no new traces can be added to update the model. The procedure typically converges within three iterations.

Further, the cross-correlation during the iteration step would measure delay times that can be used to empirically shift the traces before the next iteration. Applying the time correction would reduce impacts from heterogeneous three-dimensional (3D) velocity structures in Alaska (Feng & Ritzwoller, 2019; Jiang et al., 2018; Nayak et al., 2020). To quantify the uncertainties of the obtained CSF models, we bootstrap the set of traces that are used to obtain the final preferred models. In each bootstrap run, we randomly draw 80% of the total traces for the 2016 Lamplugh Glacier and 2017 Wrangell Mountains landslides, respectively (Figure 5 and Figure S1 in Supporting Information S1), and the same traces can be selected multiple times for a realization. We perform 500 bootstrap realizations for each landslide to obtain statistically reliable estimates of the model uncertainties.

3.3. Validating and Characterizing Landslides Using Space-Based Imagery

3.3.1. Sentinel-2 Optical Imagery

The Sentinel-2 imagery provide 10 m-resolution, true-color composite of the areas of interest. We initially select two images that most tightly bracket the event date and have minimal cloud coverage to examine the source region. When needed, we also use additional images taken during different seasons to confirm the nature of seismically detected events (e.g., discriminate landslides and snow avalanches). The optical imagery is further used to estimate the landslide area and runout distance. The full deposit imagery is useful for mass estimation, while the runout distance can provide key constraints to guide the CSF-derived trajectories (Figure 8).

3.3.2. Sentinel-1 SAR Imagery

We also use Sentinel-1 SAR data to independently classify the seismic detection and characterize the landslide parameters by examining the phase coherence and variations in the radar amplitude in the radar images taken before and after the event (Mondini et al., 2021; Yonezawa & Takeuchi, 2001). Unlike Sentinel-2 optical imagery, Sentinel-1 radar imagery is not limited by weather and light conditions (Rees, 2013). Ground motion due to a landslide can cause changes in the reflective properties of the Earth's surface, which can be manifested in variations in the radar amplitude and phase correlation. Anomalous changes in the radar amplitude can be used to map

the landslide extent (Mondini et al., 2021). We focused the raw SAR data into Single Look Complex images, and computed the radar amplitude images for each acquisition date. Images were coregistered using the BESD (Bivariate Enhanced Spectral Diversity) algorithm (Wang et al., 2017). We then subtracted the coregistered amplitude images to obtain the differential amplitude (e.g., Figure 7). We also computed phase coherence for each interferometric pair spanning the event date (e.g., Figure 9). Phase coherence is another measure of surface changes that can be used to map out the landslide area. All of the above steps are automated and can be readily applied to process SAR data covering large areas.

4. Results

We first use data from a known landslide to validate our detection procedure. Our test case is the 2016 Lamplugh Glacier landslide that occurred in Alaska.

4.1. The 2016 Lamplugh Glacier Landslide

The Lamplugh Glacier landslide generated globally detectable surface waves (Ekström, 2006; Ekström et al., 2012), originated from a north-facing bedrock ridge and ran out onto the Lamplugh Glacier (Dufresne et al., 2019). The landslide lasted 75 s, and occurred in two stages, with a total displacement of about 10 km in length and a maximum width of 3.5 km and a ratio of fall height to travel distance (H/L) of 0.15 (Dufresne et al., 2019). The event had a deposit area of about 21 km^3 and mobilized 1.4×10^{11} kg of materials (Dufresne et al., 2019). Additionally, the landslide triggered a second rock slope failure two hours later, depositing on top of the proximal rock avalanche (Dufresne et al., 2019). The 2016 Lamplugh Glacier landslide produced a coherent surface wavefield across Alaska and the contiguous United States (Figure 1a). Rayleigh waves can be easily identified from vertical velocity records that are filtered at 20–70 s period band, and the waveforms remain coherent up to 1,000 km away (Figure 2a). The event was detected by 257 triad subarrays from 354 stations. Our seismically inferred event location is 3 km away from the mountain piedmont. The nearest station, BESE, is 119 km away from the landslide, and its high-frequency record (0.1–1 s period band, vertical component) has a spindle shape without clear body wave phases (Figure 2c), which is typical for landslides. Additionally, the spectrum of BESE has a bell shaped spectrum (Figure 2e) with the first 30 s exhibiting limited high-frequency radiation, differing from typical earthquake seismograms (e.g., Gualtieri & Ekström, 2018). There is more high-frequency radiation 30 s after the event onset, which may be due to changes in the speed of the mobilized material (Dammeier et al., 2011; Deparis et al., 2008; Hibert et al., 2011; Norris, 1994).

As a validation of our CSF inversion approach, we estimate a failure model of the 2016 Lamplugh Glacier landslide using 45 traces from 25 stations (Figure 3a). The preferred CSF model can explain the seismic observations well, including traces that are not used in the CSF inversion (example traces in Figures 4a–4c, see all traces in Figure S1 in Supporting Information S1). To compare the waveform fit, the synthetic and the observed waveforms are normalized by the peak amplitude of the observation for each trace (e.g., Figure 4). The CSF model is robustly resolved as the ensemble of bootstrap models does not deviate away from the preferred model very much (gray lines in Figures 5a–5c). For each bootstrap realization, we record the normalized residual and cross-correlation (CC) coefficient of each waveform, and the median values of the CC coefficient and the median values of the residuals are around 0.6 and 0.65 for all three components, respectively (Figure S5 in Supporting Information S1). The bootstrap exercises suggests that the waveform fits of the vertical, north-south, and east-west components are comparable on average (Figure S5c in Supporting Information S1). There is no clear differences in the misfits between the north-south and east-west components despite the landslide primarily sliding northward (Figure S6 in Supporting Information S1). The CSF model suggests that the event had two downward acceleration stages and two associated deceleration stages (Figures 5a–5c). The landslide primarily slid toward north as suggested by the horizontal accelerations (Figure 6a), consistent with satellite imagery (Figure 7b; Dufresne et al., 2019). The peak centroid force is 2.55×10^{11} N, which empirically corresponds to a displaced mass of 1.34×10^{11} kg (Ekström & Stark, 2013). This mass estimate agrees well with the field survey estimate of 1.41×10^{11} kg (Dufresne et al., 2019).

The 2016 Lamplugh Glacier landslide gave rise to conspicuous changes in the backscatter characteristics of the landslide area, expressed in changes in the radar amplitude. For the 2016 Lamplugh Glacier landslide, we use data acquired on June 6 and 30 June 2016 by the Sentinel-1A satellite from the descending track 145 (absolute orbits 11,592 and 11,942) in the Interferometric Wide (IW) swath mode (Figure 7). Figure 7a shows the amplitude of

the Sentinel-1 radar image acquired on 6 June 2016, and Figure 7b shows the differential amplitude between the June 6 and June 30 acquisitions. As one can see in Figure 7b, the Earth's surface was roughened within the landslide area, resulting in an increased backscatter. The respective changes in the radar amplitude are not correlated with the preevent radar amplitude (Figure 7a). The phase coherence from the same interferometric pair is unfortunately less useful in this case because of a substantial snow cover that degraded the phase coherence over the entire scene. The differential amplitude data suggest that the landslide had a runout of ∼10 km, moving northward. The area and boundary of the landslide inferred from the SAR images (Figure 7b) are consistent with results of previous studies, which employed optical images and field surveys (Dufresne et al., 2019).

4.2. The 2017 Wrangell Mountains Landslide

Here, we report a previously unregistered event in the Wrangell Mountains region that we discovered using the AELUMA method. The event occurred on 22 September 2017 and produced coherent waveforms that were detected by 162 triad subarrays from 238 stations in Alaska and the contiguous United States (Figure 1b). We confirm that the event is a landslide by inspecting the Sentinel-2 images (Figure 8). Images from three acquisitions, dated 5 August 2017 before the seismically detected event, 20 November 2017 shortly after the event, and 23 July 2018 in the following summer, are used to investigate the Wrangell Mountains landslide (Figure 8). Initially, we used the two Sentinel-2 images obtained on August 5 and 20 November 2017. These images most tightly bracket the seismically detected event and are relatively cloud-free. Changes in surface conditions are obvious from a comparison of the two images (see areas outlined by yellow circles in Figures 8a and 8b). However, the 20 November 2017 acquisition was affected by snow cover (Figure 8b). To verify that the event was a landslide and not a snow avalanche, we inspected an image taken in the following summer (23 July 2018, Figure 8c). The landslide deposits can be clearly identified in the color composites in the image taken on 23 July 2018 (Figure 8c). A comparison of Figures 8a and 8c clearly shows the event was a landslide. The ground-truth location (Table S1 in Supporting Information S1) obtained from Sentinel-2 imagery is 5 km away from the seismically determined location. The Sentinel-2 imagery also suggests that the landslide produced two deposit piles, with the greater pile having a runout distance of 1.5 km (Figure 8c). The surface area of the two piles is about 1.6 km^2 in total.

We also verified the landslide occurrence using SAR data that were acquired on September 20 and 2 October 2017 by the Sentinel-1A satellite from the descending track 14 (absolute orbits 18,461 and 18,636) in the IW swath mode (Figure 9). The 2017 Wrangell Mountains landslide is located at the intersection of two subswaths (subswaths 2 and 3) of the Sentinel-1A track, and we used both subswaths in our analysis. The respective interferometric pair features a low phase coherence at the location suggested by the optical Sentinel-2 data. Because the location happens to be in the overlap area between two radar subswaths, the same low-coherence feature can be seen independently in each subswath (Figure 9). The radar amplitude also changes between the two acquisitions, with a higher backscatter anomaly at the landslide site (Figure S7 in Supporting Information S1). From the coherence images, the landslide area is estimated at ∼1.7 km^2 using a coherence threshold of 0.15 (Figures 9d and 9e), which is empirically selected to match the surface area resolved from the Sentinel-2 optical images.

The landslide radiated seismic waves that can be clearly identified in the period band of 20–70 s up to 1,000 km away (Figure 2b). The record section shows coherent wave packets with a move out velocity of 3.6 km/s, which is consistent with typical surface wave velocity in the period band. Station MCR2 is 26 km away from the landslide (Figure 2d), and its high-frequency (0.1–1 period band, vertical component) waveform has a spindle shape, confirming the source as a landslide. The high-frequency radiation lasted less than 100 s with two main episodes, and the second episode has a longer duration with greater amplitudes (Figure 2d). The spectrograms of the event (Figure 2f) are similar to that of the 2016 Lamplugh Glacier landslide in bell shapes (Deparis et al., 2008; Hibert et al., 2011). The seismic radiation above 5 Hz of the Wrangell Mountains landslide decayed rapidly at further distances. For example, station RH05 is 106 km away from the Wrangell Mountains landslide, similar to the separation distance between BESE and the Lamplugh Glacier landslide but its relative high-frequency content is significantly smaller compared to that of the Lamplugh Glacier landslide.

The CSF model of the Wrangell Mountains landslide suggests a multi-stage failure process (Figures 5d–5f), considerably more complex than that of the Lamplugh landslide. The model suggests a total duration of 140 s, which is 40 s longer than the high-frequency duration observed at MCR2 (Figure 2d). Multiple acceleration and deceleration stages can be identified from the vertical centroid single force history (Figure 5d). The vertical force has a comparable peak amplitude as forces at horizontal directions, indicating three-dimensional sliding

motions (Figures 5d–5f). The horizontal force histories show that the Wrangell Mountains landslide may have changed its sliding directions multiple times, different from the Lamplugh Glacier event, which mostly moved northward (Figure 7). The ensemble models from the bootstrap tests are tightly clustered around the preferred model (Figures 5d–5f). Waveform ℓ_1 residuals and the cross-correlation coefficients from the bootstrap tests have a median CC value of 0.79 and a median residual value of 0.54 for the three components. Intriguingly, the waveform fits of the north-south component have slightly lower normalized residuals on average (Figure S5 in Supporting Information S1) than those of the vertical and east-west components. As the 2017 Wrangell Mountains landslide has a complex failure history, the source excitation might have been azimuthally dependent and generated simpler waveforms at the north-south directions (e.g., Figure 4).

5. Discussion

5.1. Uncertainty and Resolution

The seismically resolved locations of the 2016 Lamplugh Glacier and 2017 Wrangell Mountains landslides are 3 and 5 km, respectively, away from their ground-truth locations (Table S1 in Supporting Information S1). Considering the ~60–150 km wavelengths of the 20–50 s period band surface waves used in the AELUMA procedure, both cases are well resolved. The location accuracy is comparable to location resolution obtained using regional seismic data for landslides in the Eastern Alps (Fuchs et al., 2018). For the two landslides reported in this study, their spatial deviations are less than the grid separation distance (0.25°; W. Fan et al., 2018). The seismically resolved location may have uncertainties due to the relative positions between the array and the event, searching grid parameterization, and the 3D velocity anomalies in Alaska, which would cause surface-wave ray paths deviating away from the great circle paths (Feng & Ritzwoller, 2019; Nayak et al., 2020). One way to evaluate the impacts of these factors is to examine the spatial structure of the searching grids that have misfit values within 125% of the minimum misfit (de Groot-Hedlin & Hedlin, 2018; W. Fan et al., 2018, 2020). The distance covariance matrix of the grids can be used to provide an empirical way to examine the location uncertainties. We find that the AELUMA locations have maximum spatial uncertainties of 227 and 51 km for the 2016 Lamplugh Glacier landslide and the 2017 Wrangell Mountains landslide, respectively. In general, the spatial uncertainties are smaller for seismic sources located within the seismic array. We emphasize that these empirical spatial uncertainties represent a conservative upper limit of location deviations, which are different from the true differences, the values can be used as an assessment of the possible impacts from factors mentioned above. The true location uncertainties are around 5 km as demonstrated using space-based measurements in this study.

The landslide CSF models are inverted from using band-limited seismic data and they best represent the macroscopic loading and unloading processes during landslide failures. Microscopic processes, such as the associated debris flow, may generate high frequency seismic radiation and are challenging to resolve with teleseismic records (Chmiel et al., 2021). The 1D velocity model used for Green's functions can capture the waveform shapes but cannot predict the surface wave arrival times accurately. To mitigate the 3D velocity influence, we apply empirical corrections before performing the inversion, which are obtained from cross-correlating the synthetic waveforms with the observations. We also examine the data influences in the CSF models by performing bootstrap resampling of the traces. The ensemble models from the bootstrap realizations are consistent with each other (Figure 5). In our method, we do not postprocess the CSF models, and the onset of a landslide is determined as the first downward acceleration and the termination yields the forces reaching zero. Due to the limited frequency bandwidth used in the inversion, small oscillations are present in the CSF models. However, they do not impact the main failure episodes very much (Figure 5). The waveform misfit is higher than typical values because we measure the ℓ_1 normalized residuals instead of the ℓ_2 normalized residuals. For comparison, our CSF model of the 2016 Lamplugh landslide is consistent with other published CSF models (Dufresne et al., 2019; Toney & Allstadt, 2021), and its failure process agrees with the surface structures resolved from field surveys (Dufresne et al., 2019).

Optical images can directly validate the seismic detections. However, weather conditions may hinder timely verification of landslides in Alaska. For example, the first clear optical image of the 2017 Wrangell Mountains landslide from Sentinel-2 was taken on 20 November 2017 and the most recent cloud-free image before the landslide was taken on 2 August 2017. The three-month separation between the two acquisitions would hamper resolving the event occurrence time if we have only used optical images. In such cases, SAR imagery can provide a complementary verification for a better temporal resolution. For example, the two SAR images collected on
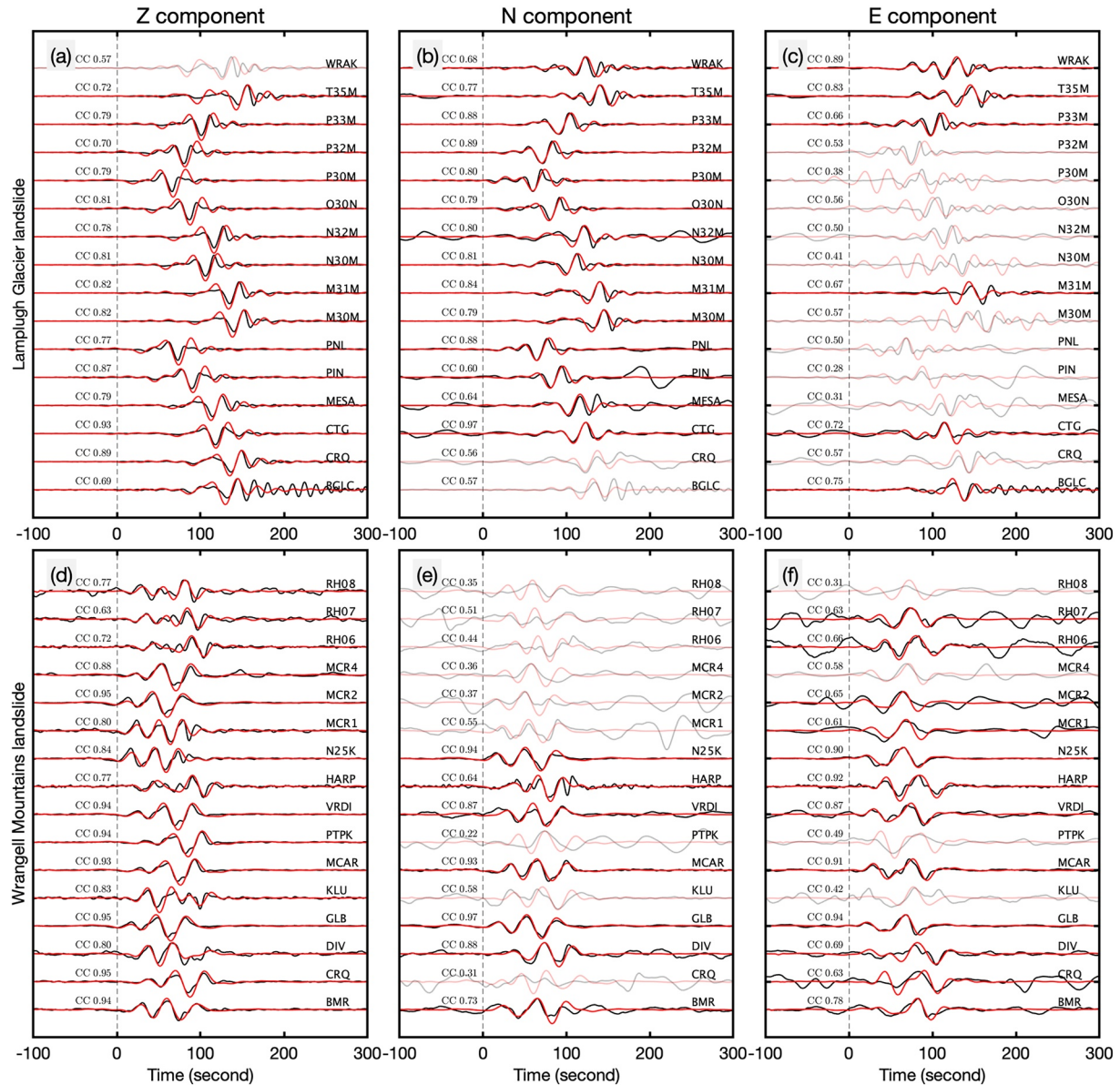
Figure 4. Example waveforms of the landslides. (a–c) Observed and synthetics seismograms of the 28 June, 2016, Lamplugh Glacier landslide. (d–f) Observed and synthetics seismograms of the 22 September, 2017 Wrangell Mountains landslide. Black and red traces are observed and synthetic seismograms, respectively. Translucent traces were not used for the centroid single force inversion. Origin times (0 s) are the onset times of the 200 s time windows. All traces used in the inversion are shown in Figures S1–S4 in Supporting Information S1.

September 20 and 2 October 2017 can provide a more timely assessment of the 2017 Wrangell Mountains land-slide (12 days separation; Figure 9). The coherence changes in the SAR images sharply delineate a region with surface alteration (circled in Figure 9). The quasi-triangular geometry of the low coherence area suggests that it is most likely caused by a landslide (Mondini et al., 2021). In contrast, the SAR amplitude changes before and after the event are ambiguous at the landslide site, and the cause of the amplitude changes is less definitive without other independent geophysical evidence (Figure S7 in Supporting Information S1). The SAR images for the 2016 Lamplugh event show the opposite sensitivities such that the differential radar amplitude works better as a proxy to identify landslides than the phase coherence (Mondini et al., 2019). The effectiveness of the phase decorrelation as a landslide marker is strongly affected by the mean coherence of the study area. If the coherence is low (e.g., due to vegetation or snow cover), a further reduction in coherence due to surface disturbance may not produce a clear anomaly. The effectiveness of the differential radar amplitude may depend on the perpendicular
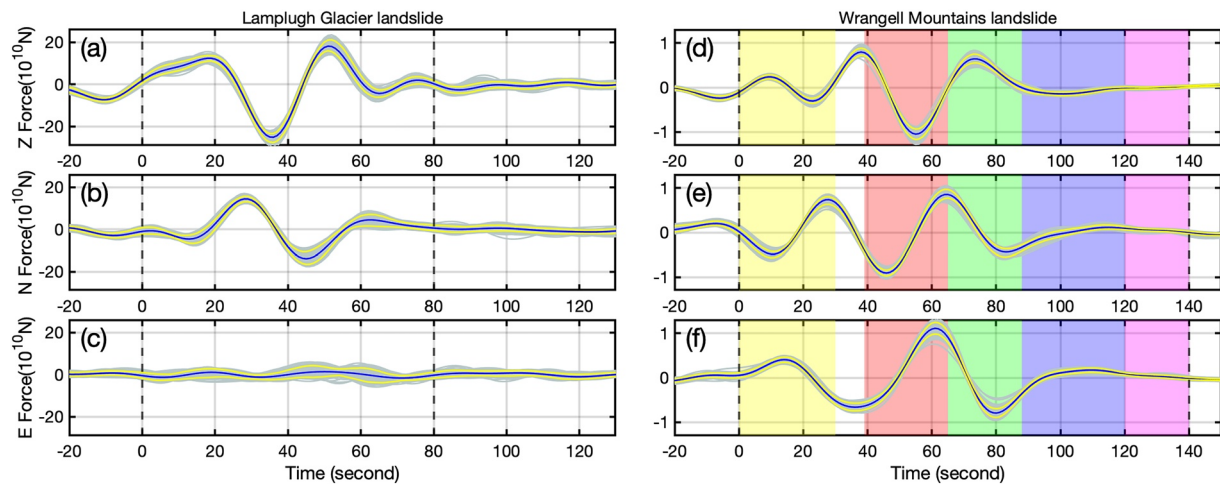
Figure 5. Three-component centroid single force (CSF) models of the 2016 Lamplugh Glacier landslide (a–c) and the 2017 Wrangell Mountains landslide (d–f). Blues lines show the preferred CSF models. Gray lines show CSF models obtained from the bootstrap resampling. Yellows lines show the 90% confidence intervals inferred from bootstrap resampling. Dash lines indicate the estimated origin and ending times of the landslides. Color patches in (d–f) sequentially show five stages of the 2017 Wrangell Mountains landslide. Time axis is relative to the CSF origin times.

baseline between the repeat orbits (Manzo et al., 2012; Mastro et al., 2022). Larger perpendicular baselines may result in higher "background" values of the differential amplitude due to somewhat different lines of sight, which can reduce the signal-to-noise ratio for the amplitude changes caused by the landslide motion. Therefore, we suggest to use both SAR measurements to evaluate possible landslide detections.

5.2. Mass Estimate of the 2017 Wrangell Mountains Landslide

The surface area of the 2017 Wrangell Mountains landslide is estimated as 1.6 km^2 using the Sentinel-2 images and 1.7 km^2 using the Sentinel-1 phase coherence anomaly (Figure 9a). The satellite images suggest that the land-slide has two branches, with the southern branch 8.4 times greater in area than the northern branch (Figure 9a). Therefore, we focus on the southern branch to estimate its mass. The observed surface alteration area likely consists of the source, sliding, and deposition areas. We assume that the mass is conserved and the landslide is a deep-seated event because of the coherent surface wavefield. In this case, if the displaced materials had
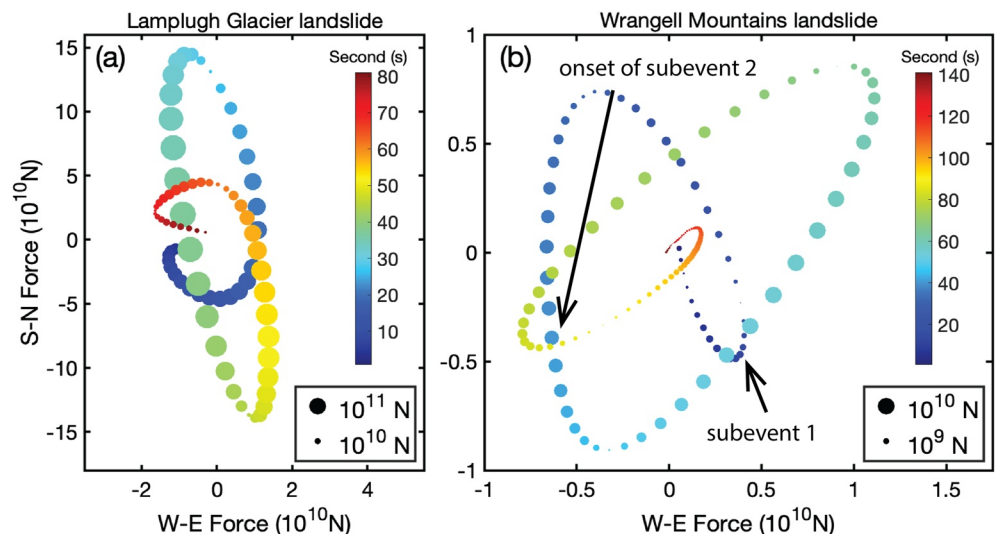

Figure 6. Horizontal centroid single force histories. (a) Lamplugh Glacier landslide. (b) Wrangell Mountains landslide. Color and size of the dots indicate the failure time and force strength. Time is relative to the CSF origin times.
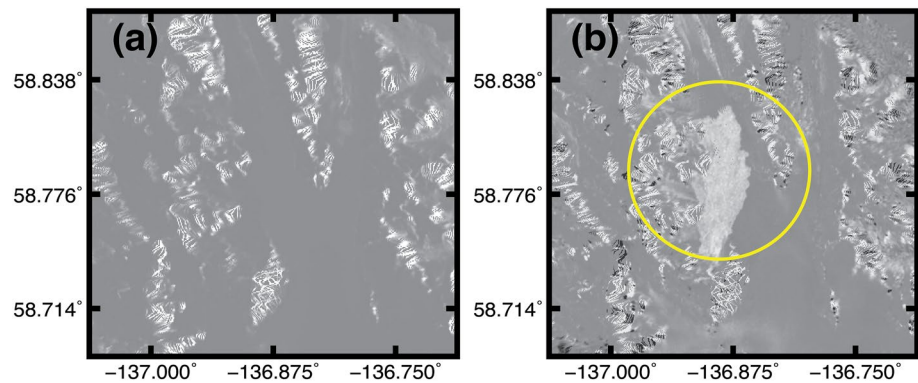
Figure 7. (a) Radar amplitude of a Sentinel-1 Synthetic Aperture Radar (SAR) image acquired on June 6 (before the 2016 Lamplugh Glacier landslide). (b) Differential radar amplitudes from two Sentinel-1 SAR images acquired on June 6 and 30. The 2016 Lamplugh Glacier landslide is outlined by the yellow circle and manifested by an increased radar backscatter. The amplitude changes do not correlate with the local topography. Note the difference in color limits between the two panels.

a thickness around 50 m at the source region (Okuwaki et al., 2021; Xu et al., 2021) with an area of 0.04 km^2 (200 m by 200 m, blue rectangle in Figure 9a), the mass estimate would be 5×10^9 kg assuming an average bedrock density of 2.5×10^3 kg/m^3 (Ridgway et al., 2007). By inspecting the Sentinel-2 image, the deposition area of the southern branch (green rectangle in Figure 9a) is estimated to be about 1.25 km^2, and the landslide mass would be 5×10^9 kg for an average thickness of 1.6 m at the deposition area. These mass estimates are based on the assumed landslide material thickness, and are subject to large uncertainties. Better constraints on the landslide thickness can be obtained for example, by differencing digital elevation models (Lin et al., 2006), provided such models are available with sufficient accuracy and resolution before and after the event.

Following the empirical scaling relationship between the maximum centroid single force and the displaced mass in Ekström and Stark (2013), the southern branch of the Wrangell Mountains landslide may have moved a total mass of 7.8×10^9 kg, and the bootstrap ensemble models suggest a variation of the mass ranging from 7.5×10^9 kg to 8.6×10^9 kg within a 90% confidence interval. Additionally, landslide duration magnitude can help constrain the mass volume (Manconi et al., 2016), although the duration magnitude computation would require region-specific coefficients for Alaska landslides (Castello et al., 2007), motivating future research for Alaska earthquakes and landslides.

We can further combine the parameters obtained from both the CSF model and space-based images for a better constrained mass estimate. The runout distance of the southern branch is estimated as about 700–1,500 m from the space-based observations, and the runout uncertainty reflects the possible range of the centroid location of the displaced mass. Given that the CSF model is the product of the displaced mass times the acceleration ($F = ma$), and the runout is the double integration of the horizontal acceleration (a_t) in the sliding direction, we can thus estimate the displaced mass from the following equation:
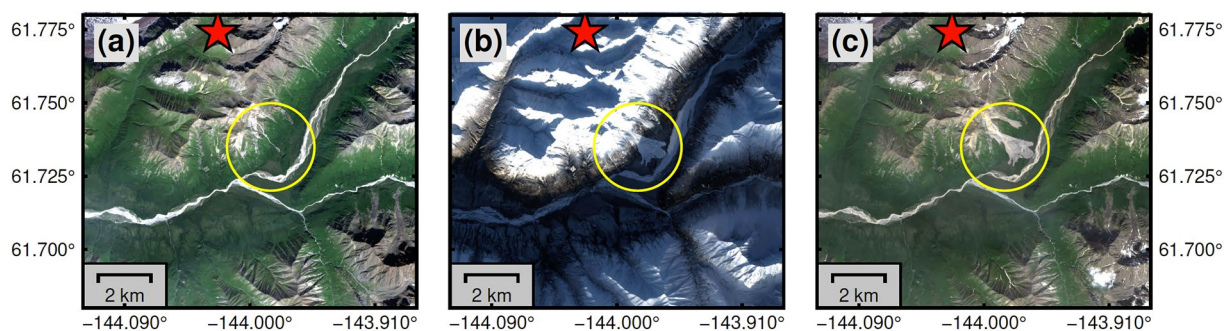

Figure 8. Sentinel-2 imagery of the 2017 Wrangell Mountains landslide. (a–c), Optical images acquired on August 5 and 20 November 2017, and 23 July, 2018. Red star shows the seismically determined location. Yellow circle indicates surface alternation caused by a landslide. The images are true color composition using bands 2–4 of Sentinel-2. Color stretching is applied to adjust image brightness.
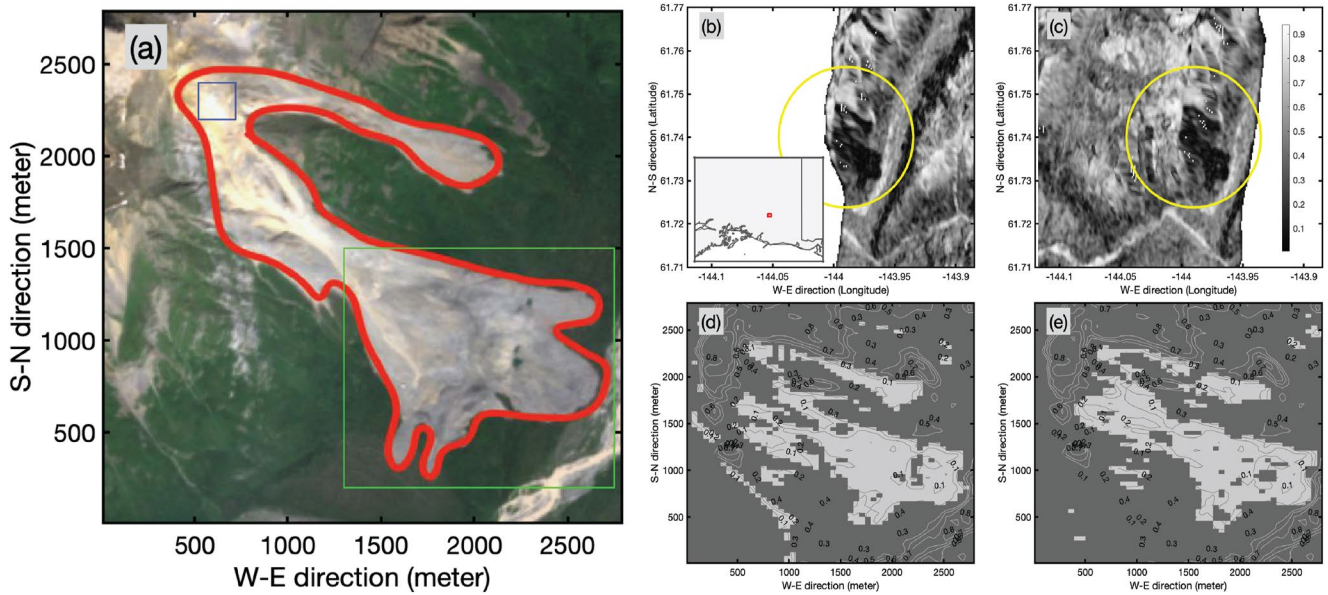
Figure 9. Area estimates of the 2017 Wrangell Mountains landslide. (a) Landslide area estimated using Sentinel-2 imagery. Red contour outlines the landslide. Thin blue box shows an assumed source area of subevent 2 and thin green box shows an assumed deposition region of subevent 2. The green box is determined based on visual inspections of the local morphology, which is also confirmed by a supervised classification exercise of the area using a random forest tree method. Sentinel-1 Phase coherence images obtained from two acquisitions on September 20 and 2 October, 2017. (b) Subswath 2. (c) Subswath 3. Low coherence regions within the yellow circle correspond to the landslide area. (d and e) Coherence image of sub-swaths 2 and 3 with a mask threshold of 0.15. Masks of Sentinel-1 Synthetic Aperture Radar coherence images obtained from two acquisitions on September 20 and 2 October, 2017. Contours show the coherence values.

$$m = \frac{\int_{t_s}^{t_e} dt \int_{t_s}^{t_e} F_t dt}{L_t},$$

(3)

where t_s and t_e are starting and terminating times of the sliding process, F_t is the horizontal force in the sliding direction, and $L_t = \int_{t_s}^{t_e} dt \int_{t_s}^{t_e} a_t dt$ is the center of mass runout distance. The horizontal force, F_t, can be obtained from the CSF model, and the runout distance can be measured from the space-based images. In practice, we forward calculate the trajectory using an assumed mass to identify the optimal value that best matches the runout distance resolved from the satellite imagery. Using the combined method, we obtain a mass estimate of $2.5–5.3 \times 10^9$ kg with the uncertainty range accounting for the runout distance uncertainties. In summary, the mass estimates from different methods are generally in agreement with each other. If we combine all the estimates, the displaced mass of the southern branch is likely in the range of $2.5–8.6 \times 10^9$ kg. The total mass of both branches is estimated in the range of $3.1–13.4 \times 10^9$ kg by evaluating the northern branch using the same set of techniques. For the following dynamic failure analysis, we take a failure mass of 1.5×10^9 kg for subevent 1 and 3.5×10^9 kg for subevent 2.

5.3. Failure Dynamics of the 2017 Wrangell Mountains Landslide

Satellite imagery from Sentinel-1 and Sentinel-2 (Figure 9) shows two separate deposits of the 2017 Wrangell Mountains landslide. However, it is unclear whether the two deposits were from the same landslide or from two separate landslides occurring within the acquisition intervals of satellite data. In the case of a single landslide scenario, the relations between the two subevents cannot be resolved using remote sensing data alone. Complementary to the imagery, the seismic CSF model can offer insights into the failure trajectory (Figure S10 in Supporting Information S1) but cannot resolve concurrent or immediate-sequential subevents for landslides because of its point source approximation.

Optical images from the Sentinel-2 satellite suggest that the source region of the 2017 Wrangell Mountains landslide is from a local mountain crest (the upper left region within the contour area in Figure 9a). The two deposits resulted from two distinct sliding trajectories with the northern branch sliding toward an azimuth of 116° and the
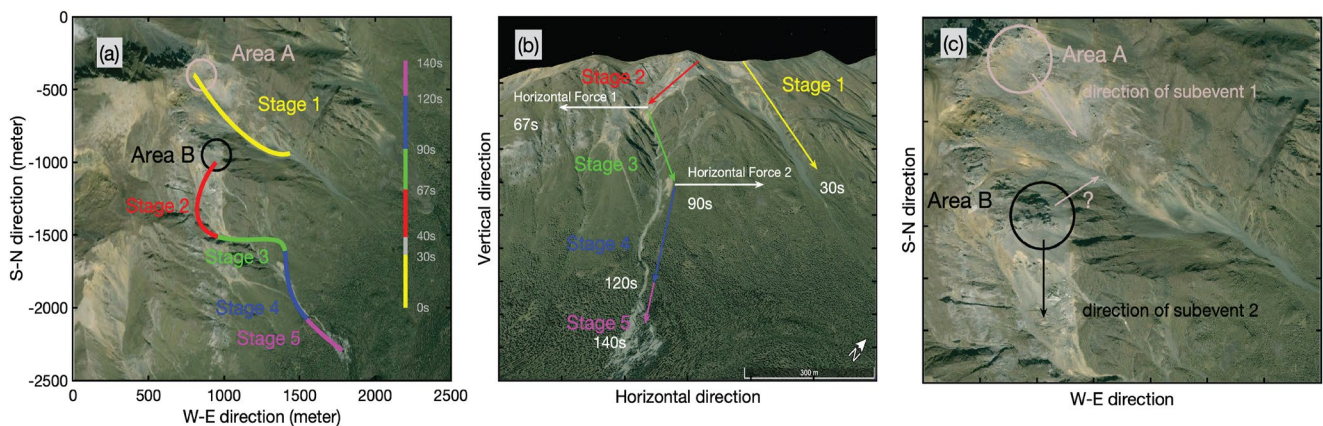
Figure 10. Inferred failure process of the 2017 Wrangell Mountains landslide. (a) Horizontal sliding trajectories of two subevents on a map-view satellite image. Colored lines represent five sliding stages with their occurrence times indicated in the color bar. Overlapping time of the two subevents from 30 to 40 s are not interpreted. (b) Schematic sliding process on an oblique-view satellite image. (c) Zoom-in view of the source areas in (a). Area A and Area B are two possible initiation sites. Black arrow shows the sliding direction of Stage 2. Pink arrows show possible sliding directions of subevent 1. Background images are from Google Earth™ taken on 4 August 2004, provided by Maxar Technologies.

southern branch sliding toward an azimuth of 175°. The CSF model indicates an initial sliding direction of 139° (Figure S10 in Supporting Information S1), which is more consistent with the trajectory of the northern branch. Therefore, the northern subevent likely occurred first. The horizontal trajectory calculated from the CSF model can only match the topographic features at the northern branch up to 30 s, while the total failure process lasted for about 140 s (Figure S10 in Supporting Information S1). The observations indicate that the southern branch may have occurred from 30 to 140 s, suggesting that the two branches were from one landslide. We denote the northern and southern branches as subevent 1 and 2, respectively.

We therefore divide the CSF model into two parts to study the spatiotemporal evolution of the two subevents. The starting time of subevent 2 is determined by comparing the CSF horizontal trajectory to the topographic features (Text S1 and Figure S10 in Supporting Information S1). The trajectory is the displacement integrated from the horizontal accelerations, which are obtained by dividing the mass estimates (1.5×10^9 kg for subevent 1, 3.5×10^9 kg for subevent 2) from the horizontal centroid single forces. The results show that the transition between the ending of subevent 1 and the initiation of subevent 2 most likely occurred at 40 s. There may have been a short overlap between the two subevents because the three-component centroid forces do not synchronize to zero at the same time, suggesting a possible concurrent ending and starting of the two subevents during 30–40 s.

While subevent 1 is relatively simple with one episode of sliding with a linear trajectory (Stage 1), subevent 2 likely had four sliding stages lasting for about 100 s (Stages 2–5 in Figures 10a and 5d–f). Subevent 2 likely initiated from Area B in Figure 10c and slid toward a direction of 185° (Stage 2). The mobilized materials hit a mountain ridge with a southeast strike at 67 s and then turned toward a direction of 94°, sliding for another 23 s (Stage 3). Bounded in a valley, the subevent was forced to turn toward 164° at 90 s again and then moved along an incision valley from 90 to 120 s (Stage 4). When the failure material reached the bottom of the mountain at 120 s, the vertical centroid single force dropped to zero due to the low topographic relief, and the runout gradually lost its momentum (Stage 5). The Stage 5 sliding caused the material to spread out in a local basin with an approximate footprint of 1.25 km² (Figure 10a). Visual inspections of the Sentinel-2 and Google Earth satellite imagery (Figures 8c and 10a) suggest a possible overshoot of the failure material at the end of Stage 2. Some landslide material may have slid beyond the ridge around 50 s.

The peak sliding velocity of subevent 2 is about 39 m/s, assuming a failure mass of 3.5×10^9 kg. The sliding velocity is comparable to the 2015 Taan Fiord and the 2016 Lamplugh Glacier landslides (e.g., Dufresne et al., 2019; Gualtieri & Ekström, 2018). The failure processes of the two subevents inferred from the CSF model (horizontal displacements) match well with the trajectories identified from morphology features using satellite images (Figure 10). The vertical displacement is not used for inferences because it does not match the elevation changes (Figures S8 and S9 in Supporting Information S1). This is not surprising as CSF models of other landslides also

have challenges in fitting the elevation changes (e.g., Toney & Allstadt, 2021; Toney et al., 2020). It is likely because the CSF model is obtained from band-limited seismic data and we used a simplistic 1D velocity model to compute the Green's functions without considering the topographic effects. The good azimuthal coverage of the network may help better resolve the horizontal CSF components in comparison to the vertical component. Additionally, the short period data (~20 s) may have further challenged the modeling efforts due to the inaccurate velocity model. Further systematical modeling exercises are warranted to investigate the observed discrepancy.

Landslides may occur frequently in the region at the same spots. The source areas (Areas A and B) identified in Figure 10c were from an optical Maxar satellite image taken in 2004, which indicates previous landslides occurring before 2004. In conjunction with the 2017 landslide, the images indicate that the slope materials have been unstable for decades, and the material and topographic conditions may favor retrogressive landslides, which propagate the failure surface upslope toward the crest. The source areas are likely covered in snow in winter times (Figure 8b) and the snow would fully melt in summer times (Figure 8c). The snowline of the Wrangell Mountains may have been retreating toward higher altitude in recent decades. The rapid changes of surface hydraulic conditions would facilitate weathering and cause material disintegration, destabilizing the mountain slope at the source areas and possibly leading to repeating landslides.

The current set of geophysical observations cannot conclusively determine the origin source region of subevent 1. The two subevents are separated by a mountain ridge, and subevent 1 could be from either Area A or B as highlighted in Figure 10c. The CSF model favors Area A as it does not indicate an initial acceleration toward the northeast direction, which would be expected if subevent 1 was from Area B. However, as shown in Figure 10c, the 2004 satellite image suggests that materials from Area B may have slipped toward the trajectory of subevent 1 in previous landslides. The relics in Figure 10c suggest that subevent 2 came from the ridge denoted as Area B. Therefore, both subevents of the 2017 Wrangell Mountains landslide may have originated from Area B as two pieces of one destabilized mass. Alternatively, subevent 1 may have originated from Area A, and its failure destabilized mass in Area B and induced subevent 2. The sequential failure of the two subevents resolved in the CSF model (Figure 10) supports this scenario. Our observations suggest that failure processes of landslides can be highly complex and multiple subevents can trigger each other to cascade into greater landslides.

5.4. Outlook on Investigating Alaska Landslides

Integrating seismic and space-based observations has proven an effective approach in detecting and locating landslides (e.g., Manconi et al., 2022; Yamada et al., 2012, 2013) and has provided insights into landslide failure mechanisms (e.g., Ekström & Stark, 2013; Walter et al., 2020; Yamada et al., 2018). The two case studies presented above show that our semiautomated workflow is highly effective in identifying Alaska landslides and revealing their failure dynamics. In particular, the 2017 Wrangell Mountains landslide is one order of magnitude smaller than the Lamplugh Glacier landslide in mass but had a more complex failure process. The 2017 Wrangell Mountains landslide is also much more complex than other recent landslides in Alaska (e.g., Gualtieri & Ekström, 2017; Toney et al., 2021). Our case study suggests that the failure processes of Alaska landslides are poorly known and emphasizes the necessity to systematically study landslides in the region. Our procedure has the potential to be applied to a large set of continuous records to efficiently identify most, if not all, of the Alaska landslides above a certain detection threshold. Specifically, we can first use the AELUMA method to systematically detect and locate abnormal seismic sources and then use SAR and optical satellite data to obtain exact locations and quantitatively evaluate surface alternations in the seismic detection areas. The seismic detection method does not require phase-picking, an accurate velocity model, or knowing the source type. The SAR data products can be obtained from a number of providers, including for example, routinely processed data products at the Alaska Satellite Facility, and the optical images are freely provided by the European Space Agency. After confirming the events as landslides, our CSF modeling procedure is computationally efficient and designed to incorporate records from seismic stations within five degrees or even further from an event. The procedure requires an analyst to select an initial set of traces, but it does not require an accurate landslide location, assuming a location error of less than 5 km as shown in this study. The location error can be corrected by the cross-correlation procedure to remove the effects of inaccurate arrival times. The inversion method iteratively update the model based on all available data within the preselected distance range. Finally, we show that combining satellite imagery and seismically determined CSF models can yield a better understanding of the landslide dynamics. For example, we combine the remote sensing data and the CSF model to infer the sequential failure process of the two 2017

Wrangell Mountains subevents, and we use the geodetic measurements of landslide runout distances to constrain integrating the CSF failure history to obtain the preferred mass estimates for the subevents.

6. Conclusions

We developed a semiautomated workflow to use seismic and space-based observations to detect and locate Alaska landslides. Taking the 2016 Lamplugh Glacier landslide as a validation case, we show that our seismically resolved location is within 3 km of the actual location ground-truthed by the remote sensing data. The 2016 Lamplugh Glacier landslide can be clearly resolved in the radar amplitude changes obtained from Sentinel-1 SAR data. Applying the AELUMA detector to continuous seismic data in 2017, we identify a previously unknown landslide in the Wrangell Mountains region. The landslide is confirmed using the Sentinel-2 optical imagery and phase coherence from Sentinel-1 data. The 2017 Wrangell Mountains landslide site is within 5 km of the seismically resolved location, demonstrating the robustness and accuracy of our procedure. We further use regional seismic records to obtain a centroid single force model of the landslide. The 2017 Wrangell Mountains landslide had two separate, sequential subevents, which involved five stages of sliding, and its dynamics were likely controlled by local terrain features. Further, satellite images suggest that the region may have landslides repeatedly occurring at the same locations. Our results demonstrate that integrating multiple geophysical methods can illuminate complex landslide failure processes in Alaska and elsewhere.

Data Availability Statement

The seismic data were provided by Data Management Center (DMC) of the Incorporated Research Institutions for Seismology (IRIS). The facilities of IRIS Data Services, and specifically the IRIS Data Management Center, were used for access to waveforms, related metadata, and derived products used in this study. Sentinel-1 data were provided by the European Space Agency (ESA) through Alaska Satellite Facility (ASF) and UNAVCO. Sentinel-2 data were provided by European Space Agency (ESA) through the Copernicus Open Access Hub website (https://scihub.copernicus.eu). The high resolution optical imagery in Figure 10 is provided by Maxar Technology through Google Earth. The seismic data were downloaded using irisFetch (https://ds.iris.edu/ds/nodes/dmc/software/downloads/irisfetch.m/2-0-12/) (Hutko et al., 2017), and the synthetic seismograms were computed using Instaseis (https://instaseis.net/) (van Driel et al., 2015). The AELUMA code can be obtained on request through IRIS (https://ds.iris.edu/ds/products/infrasound-aeluma) (Hutko et al., 2017).

References

Allstadt, K. (2013). Extracting source characteristics and dynamics of the August 2010 mount meager landslide from broadband seismograms. *Journal of Geophysical Research: Earth Surface*, *118*(3), 1472–1490. https://doi.org/10.1002/jgrf.20110

Bahavar, M., Allstadt, K. E., Van Fossen, M., Malone, S. D., & Trabant, C. (2019). Exotic seismic events catalog (ESEC) data product. *Seismological Research Letters*, *90*(3), 1355–1363. https://doi.org/10.1785/0220180402

Bardet, J.-P., Synolakis, C. E., Davies, H. L., Imamura, F., & Okal, E. A. (2003). Landslide tsunamis: Recent findings and research directions. In *Landslide tsunamis: Recent findings and research directions* (pp. 1793–1809).

Benda, L., & Dunne, T. (1997). Stochastic forcing of sediment supply to channel networks from landsliding and debris flow. *Water Resources Research*, *33*(12), 2849–2863. https://doi.org/10.1029/97wr02388

Bessette-Kirton, E. K., Coe, J. A., & Zhou, W. (2018). Using stereo satellite imagery to account for ablation, entrainment, and compaction in volume calculations for rock avalanches on glaciers: Application to the 2016 Lamplugh rock avalanche in Glacier Bay national park, Alaska. *Journal of Geophysical Research: Earth Surface*, *123*(4), 622–641. https://doi.org/10.1002/2017jf004512

Brodsky, E. E., Gordeev, E., & Kanamori, H. (2003). Landslide basal friction as measured by seismic waves. *Geophysical Research Letters*, *30*(24), 2236. https://doi.org/10.1029/2003gl018485

Castello, B., Olivieri, M., & Selvaggi, G. (2007). Local and duration magnitude determination for the Italian earthquake catalog, 1981–2002. *Bulletin of the Seismological Society of America*, *97*(1B), 128–139. https://doi.org/10.1785/0120050258

Chmiel, M., Walter, F., Wenner, M., Zhang, Z., McArdell, B. W., & Hibert, C. (2021). Machine learning improves debris flow warning. *Geophysical Research Letters*, *48*(3), e2020GL090874. https://doi.org/10.1029/2020gl090874

Coe, J. A., Bessette-Kirton, E. K., & Geertsema, M. (2018). Increasing rock-avalanche size and mobility in Glacier Bay national park and preserve, Alaska detected from 1984 to 2016 Landsat imagery. *Landslides*, *15*(3), 393–407. https://doi.org/10.1007/s10346-017-0879-7

Colesanti, C., & Wasowski, J. (2006). Investigating landslides with space-borne synthetic aperture radar (SAR) interferometry. *Engineering Geology*, *88*(3–4), 173–199. https://doi.org/10.1016/j.enggeo.2006.09.013

Dammeier, F., Moore, J. R., Haslinger, F., & Loew, S. (2011). Characterization of alpine rockslides using statistical analysis of seismic signals. *Journal of Geophysical Research*, *116*(F4), F04024. https://doi.org/10.1029/2011jf002037

de Groot-Hedlin, C. D., & Hedlin, M. A. (2015). A method for detecting and locating geophysical events using groups of arrays. *Geophysical Journal International*, *203*(2), 960–971. https://doi.org/10.1093/gji/ggv345

de Groot-Hedlin, C. D., & Hedlin, M. A. (2018). *A new automated approach to detecting and locating seismic events using data from a large network*. Bulletin of the Seismological Society of America.

Delbridge, B. G., Bürgmann, R., Fielding, E., Hensley, S., & Schulz, W. H. (2016). Three-dimensional surface deformation derived from airborne interferometric UAVSAR: Application to the slumgullion landslide. *Journal of Geophysical Research: Solid Earth*, *121*(5), 3951–3977. https://doi.org/10.1002/2015jb012559

Deparis, J., Jongmans, D., Cotton, F., Baillet, L., Thouvenot, F., & Hantz, D. (2008). Analysis of rock-fall and rock-fall avalanche seismograms in the French Alps. *Bulletin of the Seismological Society of America*, *98*(4), 1781–1796. https://doi.org/10.1785/0120070082

Doi, I., & Maeda, T. (2020). Landslide characteristics revealed by high-frequency seismic waves from the 2017 landslide in central Japan. *Seismological Society of America*, *91*(5), 2719–2729. https://doi.org/10.1785/0220200032

Dufresne, A., Geertsema, M., Shugar, D., Koppes, M., Higman, B., Haeussler, P., et al. (2018). Sedimentology and geomorphology of a large tsunamigenic landslide, Taan fiord, Alaska. *Sedimentary Geology*, *364*, 302–318. https://doi.org/10.1016/j.sedgeo.2017.10.004

Dufresne, A., Wolken, G., Hibert, C., Bessette-Kirton, E., Coe, J. A., Geertsema, M., & Ekström, G. (2019). The 2016 Lamplugh rock avalanche, Alaska: Deposit structures and emplacement dynamics. *Landslides*, *16*(12), 2301–2319. https://doi.org/10.1007/s10346-019-01225-4

Eissler, H. K., & Kanamori, H. (1987). A single-force model for the 1975 Kalapana, Hawaii, earthquake. *Journal of Geophysical Research*, *92*(B6), 4827–4836. https://doi.org/10.1029/jb092ib06p04827

Ekström, G. (2006). Global detection and location of seismic sources by using surface waves. *Bulletin of the Seismological Society of America*, *96*(4A), 1201–1212. https://doi.org/10.1785/0120050175

Ekström, G., Nettles, M., & Dziewoński, A. (2012). The global CMT project 2004–2010: Centroid-moment tensors for 13,017 earthquakes. *Physics of the Earth and Planetary Interiors*, *200*, 1–9. https://doi.org/10.1016/j.pepi.2012.04.002

Ekström, G., & Stark, C. P. (2013). Simple scaling of catastrophic landslide dynamics. *Science*, *339*(6126), 1416–1419. https://doi.org/10.1126/science.1232887

Fan, W., de Groot Hedlin, C. D., Hedlin, M. A. H., & Ma, Z. (2018). Using surface waves recorded by a large mesh of three-element arrays to detect and locate disparate seismic sources. *Geophysical Journal International*, *215*(2), 942–958. https://doi.org/10.1093/gji/ggy316

Fan, W., McGuire, J. J., de Groot-Hedlin, C. D., Hedlin, M. A., Coats, S., & Fiedler, J. W. (2019). Stormquakes. *Geophysical Research Letters*, *46*(22), 12909–12918. https://doi.org/10.1029/2019gl084217

Fan, W., McGuire, J. J., & Shearer, P. M. (2020). Abundant spontaneous and dynamically triggered submarine landslides in the Gulf of Mexico. *Geophysical Research Letters*, *47*(12), e2020GL087213. https://doi.org/10.1029/2020gl087213

Fan, W., Shearer, P. M., & Gerstoft, P. (2014). Kinematic earthquake rupture inversion in the frequency domain. *Geophysical Journal International*, *199*(2), 1138–1160. https://doi.org/10.1093/gji/ggu319

Fan, X., Xu, Q., Scaringi, G., Dai, L., Li, W., Dong, X., et al. (2017). Failure mechanism and kinematics of the deadly June 24th 2017 Xinmo landslide, Maoxian, Sichuan, China. *Landslides*, *14*(6), 2129–2146. https://doi.org/10.1007/s10346-017-0907-7

Feng, L., & Ritzwoller, M. H. (2019). A 3-D shear velocity model of the crust and uppermost mantle beneath Alaska including apparent radial anisotropy. *Journal of Geophysical Research: Solid Earth*, *124*(10), 10468–10497. https://doi.org/10.1029/2019jb018122

Froude, M. J., & Petley, D. N. (2018). Global fatal landslide occurrence from 2004 to 2016. *Natural Hazards and Earth System Sciences*, *18*(8), 2161–2181. https://doi.org/10.5194/nhess-18-2161-2018

Fruneau, B., Achache, J., & Delacourt, C. (1996). Observation and modelling of the Saint-Etienne-de-tinée landslide using SAR interferometry. *Tectonophysics*, *265*(3–4), 181–190. https://doi.org/10.1016/s0040-1951(96)00047-9

Fuchs, F., Lenhardt, W., Bokelmann, G., & AlpArray Working Group. (2018). Seismic detection of rockslides at regional scale: Examples from the eastern Alps and feasibility of kurtosis-based event location. *Earth Surface Dynamics*, *6*(4), 955–970. https://doi.org/10.5194/esurf-6-955-2018

Fukao, Y. (1995). Single-force representation of earthquakes due to landslides or the collapse of caverns. *Geophysical Journal International*, *122*(1), 243–248. https://doi.org/10.1111/j.1365-246x.1995.tb03551.x

Gomberg, J., Bodin, P., Savage, W., & Jackson, M. E. (1995). Landslide faults and tectonic faults, analogs?: The Slumgullion earthflow, Colorado. *Geology*, *23*(1), 41–44. https://doi.org/10.1130/0091-7613(1995)023<0041:lfatfa>2.3.co;2

Gomi, T., Sidle, R. C., & Richardson, J. S. (2002). Understanding processes and downstream linkages of headwater systems: Headwaters differ from downstream reaches by their close coupling to hillslope processes, more temporal and spatial variation, and their need for different means of protection from land use. *BioScience*, *52*(10), 905–916. https://doi.org/10.1641/0006-3568(2002)052[0905:upadlo]2.0.co;2

Grant, M., & Boyd, S. (2008). Graph implementations for nonsmooth convex programs. In V. Blondel, S. Boyd, & H. Kimura (Eds.), *Recent advances in learning and control* (pp. 95–110). Springer-Verlag Limited.

Grant, M., & Boyd, S. (2014). CVX: Matlab software for disciplined convex programming, version 2.1.

Gualtieri, L., & Ekström, G. (2017). Seismic reconstruction of the 2012 palisades rockfall using the analytical solution to lamb's problem. *Bulletin of the Seismological Society of America*, *107*(1), 63–71. https://doi.org/10.1785/0120160238

Gualtieri, L., & Ekström, G. (2018). Broad-band seismic analysis and modeling of the 2015 Taan fjord, Alaska landslide using instaseis. *Geophysical Journal International*, *213*(3), 1912–1923. https://doi.org/10.1093/gji/ggy086

Guthrie, R., Friele, P., Allstadt, K., Roberts, N., Evans, S., Delaney, K., et al. (2012). The 6 august 2010 mount meager rock slide-debris flow, Coast Mountains, British Columbia: Characteristics, dynamics, and implications for hazard and risk assessment. *Natural Hazards and Earth System Sciences*, *12*(5), 1277–1294. https://doi.org/10.5194/nhess-12-1277-2012

Hibert, C., Mangeney, A., Grandjean, G., & Shapiro, N. (2011). Slope instabilities in dolomieu crater, réunion island: From seismic signals to rockfall characteristics. *Journal of Geophysical Research*, *116*(F4), F04032. https://doi.org/10.1029/2011jf002038

Hibert, C., Stark, C., & Ekström, G. (2015). Dynamics of the Oso-Steelhead landslide from broadband seismic analysis. *Natural Hazards and Earth System Sciences*, *15*(6), 1265–1273. https://doi.org/10.5194/nhess-15-1265-2015

Higman, B., Shugar, D. H., Stark, C. P., Ekström, G., Koppes, M. N., Lynett, P., et al. (2018). The 2015 landslide and tsunami in Taan fiord, Alaska. *Scientific Reports*, *8*(1), 1–12. https://doi.org/10.1038/s41598-018-30475-w

Hu, X., Bürgmann, R., Lu, Z., Handwerger, A. L., Wang, T., & Miao, R. (2019). Mobility, thickness, and hydraulic diffusivity of the slow-moving Monroe landslide in California revealed by l-band satellite radar interferometry. *Journal of Geophysical Research: Solid Earth*, *124*(7), 7504–7518. https://doi.org/10.1029/2019jb017560

Hutko, A. R., Bahavar, M., Trabant, C., Weekly, R. T., Fossen, M. V., & Ahern, T. (2017). Data products at the IRIS-DMC: Growth and usage. *Seismological Research Letters*, *88*(3), 892–903. https://doi.org/10.1785/0220160190

Imaizumi, F., & Sidle, R. C. (2007). Linkage of sediment supply and transport processes in Miyagawa Dam catchment, Japan. *Journal of Geophysical Research*, *112*(F3), F03012. https://doi.org/10.1029/2006jf000495

Intrieri, E., Raspini, F., Fumagalli, A., Lu, P., Del Conte, S., Farina, P., et al. (2018). The Maoxian landslide as seen from space: Detecting precursors of failure with sentinel-1 data. *Landslides*, *15*(1), 123–133. https://doi.org/10.1007/s10346-017-0915-7

Iverson, R. M., Reid, M., Iverson, N. R., LaHusen, R., Logan, M., Mann, J., & Brien, D. (2000). Acute sensitivity of landslide rates to initial soil porosity. *Science*, *290*(5491), 513–516. https://doi.org/10.1126/science.290.5491.513

Jiang, C., Schmandt, B., Ward, K. M., Lin, F.-C., & Worthington, L. L. (2018). Upper mantle seismic structure of Alaska from Rayleigh and S wave tomography. *Geophysical Research Letters*, *45*(19), 10–350. https://doi.org/10.1029/2018gl079406

Jin, Z., & Fialko, Y. (2020). Finite slip models of the 2019 Ridgecrest earthquake sequence constrained by space geodetic data and aftershock locations. *Bulletin of the Seismological Society of America*, *110*(4), 1660–1679. https://doi.org/10.1785/0120200060

Kanamori, H., & Given, J. W. (1982). Analysis of long-period seismic waves excited by the May 18, 1980, eruption of Mount St. Helens—A terrestrial monopole? *Journal of Geophysical Research*, *87*(B7), 5422–5432. https://doi.org/10.1029/jb087ib07p05422

Kawakatsu, H. (1989). Centroid single force inversion of seismic waves generated by landslides. *Journal of Geophysical Research*, *94*(B9), 12363–12374. https://doi.org/10.1029/jb094ib09p12363

Kirschbaum, D., Stanley, T., & Zhou, Y. (2015). Spatial and temporal analysis of a global landslide catalog. *Geomorphology*, *249*, 4–15. https://doi.org/10.1016/j.geomorph.2015.03.016

Korup, O. (2005). Geomorphic imprint of landslides on alpine river systems, southwest New Zealand. *Earth Surface Processes and Landforms*, *30*(7), 783–800. https://doi.org/10.1002/esp.1171

Korup, O., Clague, J. J., Hermanns, R. L., Hewitt, K., Strom, A. L., & Weidinger, J. T. (2007). Giant landslides, topography, and erosion. *Earth and Planetary Science Letters*, *261*(3–4), 578–589. https://doi.org/10.1016/j.epsl.2007.07.025

Lacroix, P., Bièvre, G., Pathier, E., Kniess, U., & Jongmans, D. (2018). Use of sentinel-2 images for the detection of precursory motions before landslide failures. *Remote Sensing of Environment*, *215*, 507–516. https://doi.org/10.1016/j.rse.2018.03.042

Lai, V. H., Tsai, V. C., Lamb, M. P., Ulizio, T. P., & Beer, A. R. (2018). The seismic signature of debris flows: Flow mechanics and early warning at Montecito, California. *Geophysical Research Letters*, *45*(11), 5528–5535. https://doi.org/10.1029/2018gl077683

Lin, G., Shearer, P. M., & Fialko, Y. (2006). Obtaining absolute locations for quarry seismicity using remote sensing data. *Bulletin of the Seismological Society of America*, *96*(2), 722–728. https://doi.org/10.1785/0120050146

Manconi, A., Mondini, A. C., & AlpArray working group. (2022). Landslides caught on seismic networks and satellite radars. *Natural Hazards and Earth System Sciences*, *22*(5), 1655–1664. https://doi.org/10.5194/nhess-22-1655-2022

Manconi, A., Picozzi, M., Coviello, V., De Santis, F., & Elia, L. (2016). Real-time detection, location, and characterization of rockslides using broadband regional seismic networks. *Geophysical Research Letters*, *43*(13), 6960–6967. https://doi.org/10.1002/2016gl069572

Manzo, M., Fialko, Y., Casu, F., Pepe, A., & Lanari, R. (2012). A quantitative assessment of DInSAR measurements of interseismic deformation: The Southern San Andreas Fault case study. *Pure and Applied Geophysics*, *168*, 195–210.

Mastro, P., Masiello, G., Serio, C., & Pepe, A. (2022). Change detection techniques with synthetic aperture radar images: Experiments with random forests and sentinel-1 observations. *Remote Sensing*, *14*(14), 3323. https://doi.org/10.3390/rs14143323

Milillo, P., Fielding, E. J., Shulz, W. H., Delbridge, B., & Burgmann, R. (2014). Cosmo-skymed spotlight interferometry over rural areas: The slumgullion landslide in Colorado, USA. *Ieee Journal of Selected Topics in Applied Earth Observations and Remote Sensing*, *7*(7), 2919–2926. https://doi.org/10.1109/jstars.2014.2345664

Mondini, A. C., Guzzetti, F., Chang, K.-T., Monserrat, O., Martha, T. R., & Manconi, A. (2021). Landslide failures detection and mapping using synthetic aperture radar: Past, present and future. *Earth-Science Reviews*, *216*, 103574. https://doi.org/10.1016/j.earscirev.2021.103574

Mondini, A. C., Santangelo, M., Rocchetti, M., Rossetto, E., Manconi, A., & Monserrat, O. (2019). Sentinel-1 SAR amplitude imagery for rapid landslide detection. *Remote Sensing*, *11*(7), 760. https://doi.org/10.3390/rs11070760

Nayak, A., Eberhart-Phillips, D., Ruppert, N. A., Fang, H., Moore, M. M., Tape, C., et al. (2020). 3D seismic velocity models for Alaska from joint tomographic inversion of body-wave and surface-wave data. *Seismological Research Letters*, *91*(6), 3106–3119. https://doi.org/10.1785/0220200214

Nissen-Meyer, T., Driel, M. v., Stähler, S., Hosseini, K., Hempel, S., Auer, L., et al. (2014). Axisem: Broadband 3-D seismic wavefields in axisymmetric media. *Solid Earth*, *5*(1), 425–445. https://doi.org/10.5194/se-5-425-2014

Norris, R. D. (1994). Seismicity of rockfalls and avalanches at three Cascade Range volcanoes: Implications for seismic detection of hazardous mass movements. *Bulletin of the Seismological Society of America*, *84*(6), 1925–1939.

Okuwaki, R., Fan, W., Yamada, M., Osawa, H., & Wright, T. J. (2021). Identifying landslides from continuous seismic surface waves: A case study of multiple small-scale landslides triggered by typhoon Talas, 2011. *Geophysical Journal International*, *226*(2), 729–741. https://doi.org/10.1093/gji/ggab129

Petley, D. (2012). Global patterns of loss of life from landslides. *Geology*, *40*(10), 927–930. https://doi.org/10.1130/g33217.1

Poli, P. (2017). Creep and slip: Seismic precursors to the Nuugaatsiaq landslide (Greenland). *Geophysical Research Letters*, *44*(17), 8832–8836. https://doi.org/10.1002/2017gl075039

Qu, F., Qiu, H., Sun, H., & Tang, M. (2021). Post-failure landslide change detection and analysis using optical satellite sentinel-2 images. *Landslides*, *18*(1), 447–455. https://doi.org/10.1007/s10346-020-01498-0

Rees, W. G. (2013). *Physical principles of remote sensing*. Cambridge university press.

Ridgway, K., Trop, J., Glen, J., & O'Neill, J. (2007). Tectonic growth of a collisional continental margin: Crustal evolution of southern Alaska.

Sandwell, D., Mellors, R., Tong, X., Wei, M., & Wessel, P. (2011). Open radar interferometry software for mapping surface deformation. *Eos, Transactions American Geophysical Union*, *92*(28), 234. https://doi.org/10.1029/2011eo280002

Singhroy, V., Mattar, K., & Gray, A. (1998). Landslide characterisation in Canada using interferometric SAR and combined SAR and tm images. *Advances in Space Research*, *21*(3), 465–476. https://doi.org/10.1016/s0273-1177(97)00882-x

Toney, L., & Allstadt, K. E. (2021). Isforce: A python-based single-force seismic inversion framework for massive landslides. *Seismological Society of America*, *92*(4), 2610–2626. https://doi.org/10.1785/0220210004

Toney, L., Fee, D., Allstadt, K. E., Haney, M., & Matoza, R. S. (2020). Reconstructing the dynamics of the highly-similar May 2016 and June 2019 iliamna volcano, Alaska ice–rock avalanches from seismoacoustic data. *Earth Surface Dynamics Discussions*, 1–32.

Toney, L., Fee, D., Allstadt, K. E., Haney, M. M., & Matoza, R. S. (2021). Reconstructing the dynamics of the highly similar May 2016 and June 2019 iliamna volcano (Alaska) ice–rock avalanches from seismoacoustic data. *Earth Surface Dynamics*, *9*(2), 271–293. https://doi.org/10.5194/esurf-9-271-2021

Tymofyeyeva, E., Fialko, Y., Jiang, J., Xu, X., Sandwell, D., Bilham, R., et al. (2019). Slow slip event on the southern San Andreas Fault triggered by the 2017 M_w8.2 Chiapas (Mexico) earthquake. *Journal of Geophysical Research*, *124*(9), 9956–9975. https://doi.org/10.1029/2018jb016765

van Driel, M., Krischer, L., Stähler, S. C., Hosseini, K., & Nissen-Meyer, T. (2015). Instaseis: Instant global seismograms based on a broadband waveform database. *Solid Earth*, *6*(2), 701–717. https://doi.org/10.5194/se-6-701-2015

Walter, F., Amann, F., Kos, A., Kenner, R., Phillips, M., de Preux, A., et al. (2020). Direct observations of a three million cubic meter rock-slope collapse with almost immediate initiation of ensuing debris flows. *Geomorphology*, *351*, 106933. https://doi.org/10.1016/j.geomorph.2019.106933

Wang, K., Xu, X., & Fialko, Y. (2017). Improving burst alignment in TOPS interferometry with bivariate enhanced spectral diversity (BESD). *IEEE Geoscience and Remote Sensing Letters*, *14*(12), 2423–2427. https://doi.org/10.1109/lgrs.2017.2767575

Xie, J., Chu, R., & Ni, S. (2020). Relocation of the 17 June 2017 Nuugaatsiaq (Greenland) landslide based on green's functions from ambient seismic noises. *Journal of Geophysical Research: Solid Earth*, *125*(5), e2019JB018947. https://doi.org/10.1029/2019jb018947

Xu, Y., George, D. L., Kim, J., Lu, Z., Riley, M., Griffin, T., & de la Fuente, J. (2021). Landslide monitoring and runout hazard assessment by integrating multi-source remote sensing and numerical models: An application to the gold basin landslide complex, northern Washington. *Landslides*, *18*(3), 1131–1141. https://doi.org/10.1007/s10346-020-01533-0

Yamada, M., Kumagai, H., Matsushi, Y., & Matsuzawa, T. (2013). Dynamic landslide processes revealed by broadband seismic records. *Geophysical Research Letters*, *40*(12), 2998–3002. https://doi.org/10.1002/grl.50437

Yamada, M., Mangeney, A., Matsushi, Y., & Matsuzawa, T. (2018). Estimation of dynamic friction and movement history of large landslides. *Landslides*, *15*(10), 1963–1974. https://doi.org/10.1007/s10346-018-1002-4

Yamada, M., Matsushi, Y., Chigira, M., & Mori, J. (2012). Seismic recordings of landslides caused by typhoon Talas (2011), Japan. *Geophysical Research Letters*, *39*(13). https://doi.org/10.1029/2012gl052174

Yonezawa, C., & Takeuchi, S. (2001). Decorrelation of SAR data by urban damages caused by the 1995 Hyogoken-nanbu earthquake. *International Journal of Remote Sensing*, *22*(8), 1585–1600. https://doi.org/10.1080/01431160118187

1 # Supporting Information for "A joint seismic and
2 # space-based investigation of the 2016 Lamplugh Glacier
3 # and 2017 Wrangell Mountains (Alaska) landslides"

4 **Xinyu Luo[1], Wenyuan Fan[1], & Yuri Fialko[1]**

5 [1]Scripps Institution of Oceanography, University of California, San Diego, La Jolla, California, USA

6 ## Contents of this file

Text S1: Subevents of the 2017 Wrangell Mountains landslide

We use local topographic features to constrain the sliding process of the 2017 Wrangell Mountains landslide (e.g., Crowley et al., 2003; Gualtieri & Ekström, 2018). The runout of subevent 1 observed in the satellite images matches the horizontal displacement integrated up to 30 s. Subevent 1 likely ended before 40 s because the remaining trajectory matches the topography of subevent 2 precisely if its occurrence starts on 40 s (Figure S10). The results suggest no significant amount of forces from subevent 1 after 40 s. Additionally, the southward trajectory after 40 s cannot be explained by the topography of the incision valley near subevent 1 (Figure S10). However, such a direction can be explained by the topography near subevent 2. The two subevents may have overlapped because the three-component centroid signal forces do not synchronize to zero in between 30 to 40 s.

Tables S1 to S4

Table S1. Landslide centroid locations

	2016 Lamplugh landslide	2017 Wrangell Mountains landslide
AELUMA location	58.8046N;136.9087W	61.5258N;143.8212W
AELUMA time	16:20:53 UTC	09:43:11 UTC
Space-based location	58.7654N;136.8936W	61.7398N;143.9786W

Table S2. Maximum centroid single forces and mass estimation following Ekström and Stark (2013) for the 2017 Wrangell Mountains landslide

	Subevent 1	Subevent 2	Total
Maximum force	0.864×10^{10} N	1.448×10^{10} N	
Mass estimate	4.66×10^9 kg	7.82×10^9 kg	12.48×10^9 kg
90% confidence interval, maximum force	$0.831/0.891 \times 10^{10}$ N	$1.392/1.583 \times 10^{10}$ N	
90% confidence interval, mass estimate	$4.49/4.81 \times 10^9$ kg	$7.52/8.55 \times 10^9$ kg	$12.01/13.36 \times 10^9$ kg

Table S3. Mass estimate based on geodetic and seismc observations for the 2017 Wrangell Mountains landslide

	Subevent 1	Subevent 2	Total
Mass runout distance	600 m	1000 m	
Mass estimate	1.5×10^9 kg	3.5×10^9 kg	5.0×10^9 kg
Mass runout range	$300 - 1500$ m	$700 - 1500$ m	
Mass estimate range	$0.6/3 \times 10^9$ kg	$2.5/5.3 \times 10^9$ kg	$3.1/8.3 \times 10^9$ kg

Table S4. Mass estimate based on area and thickness for the 2017 Wrangell Mountains landslide

	Subevent 1	Subevent 2	Total
Total area	0.23 km^2	1.47 km^2	1.70 km^2
Source area	0.01 km^2	0.04 km^2	0.05 km^2
Passage area	0.05 km^2	0.18 km^2	0.23 km^2
Deposition area	0.17 km^2	1.25 km^2	1.43 km^2
Assumed source thickness	50 m	50 m	
Assumed deposition thickness	1.6 m	2.9 m	
Assumed density	2.5×10^3 kg/m^3	2.5×10^3 kg/m^3	
Mass estimate	1.25×10^9 kg	5.01×10^9 kg	6.25×10^9 kg

23 **Figures S1 to S11**
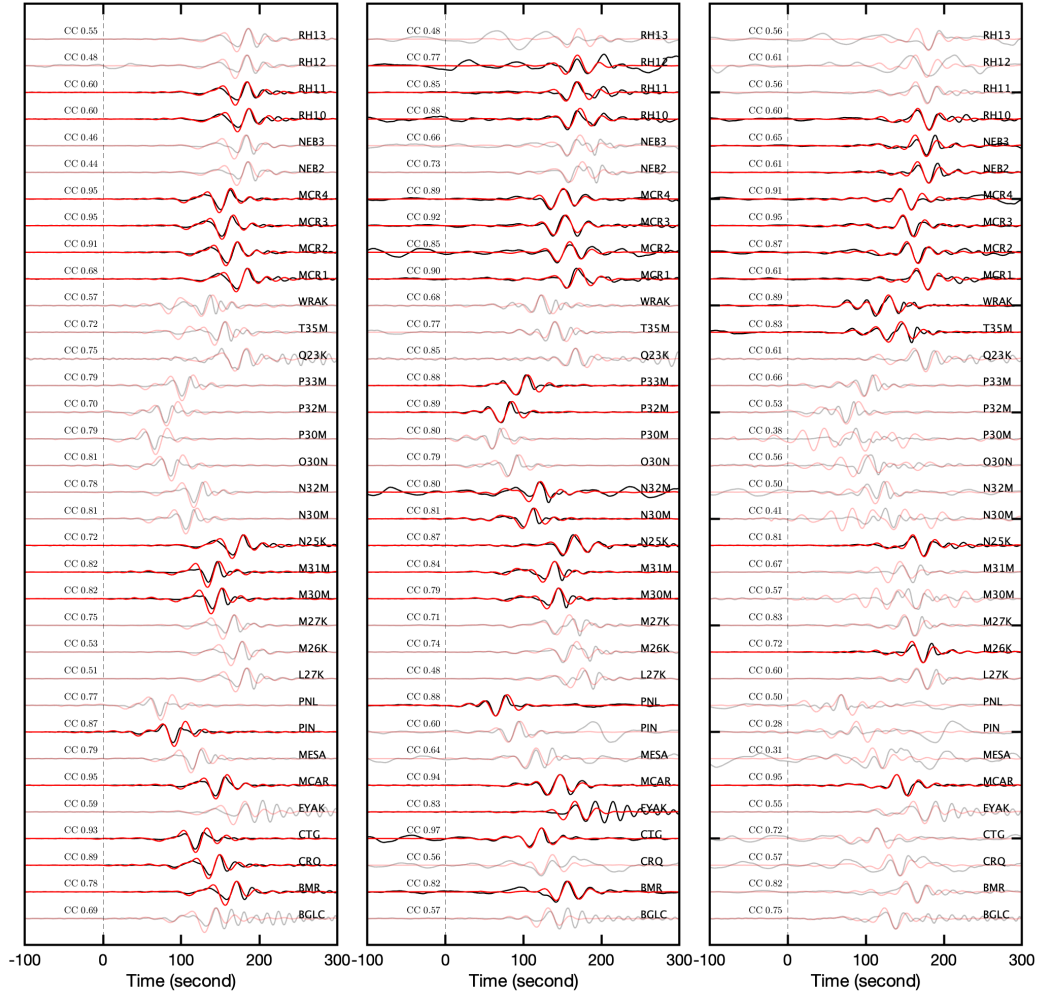
Figure S1. Observed and synthetic seismograms of the June 28, 2016 Lamplugh Glacier landslide for stations within five-degree epicentral distance. Black and red lines are the observed and synthetic seismograms, respectively. Opaque traces were not included in the centroid single force inversion. Left to right columns are for the vertical, north, and east components, respectively. Cross-correlation coefficients and station names are listed above the traces.
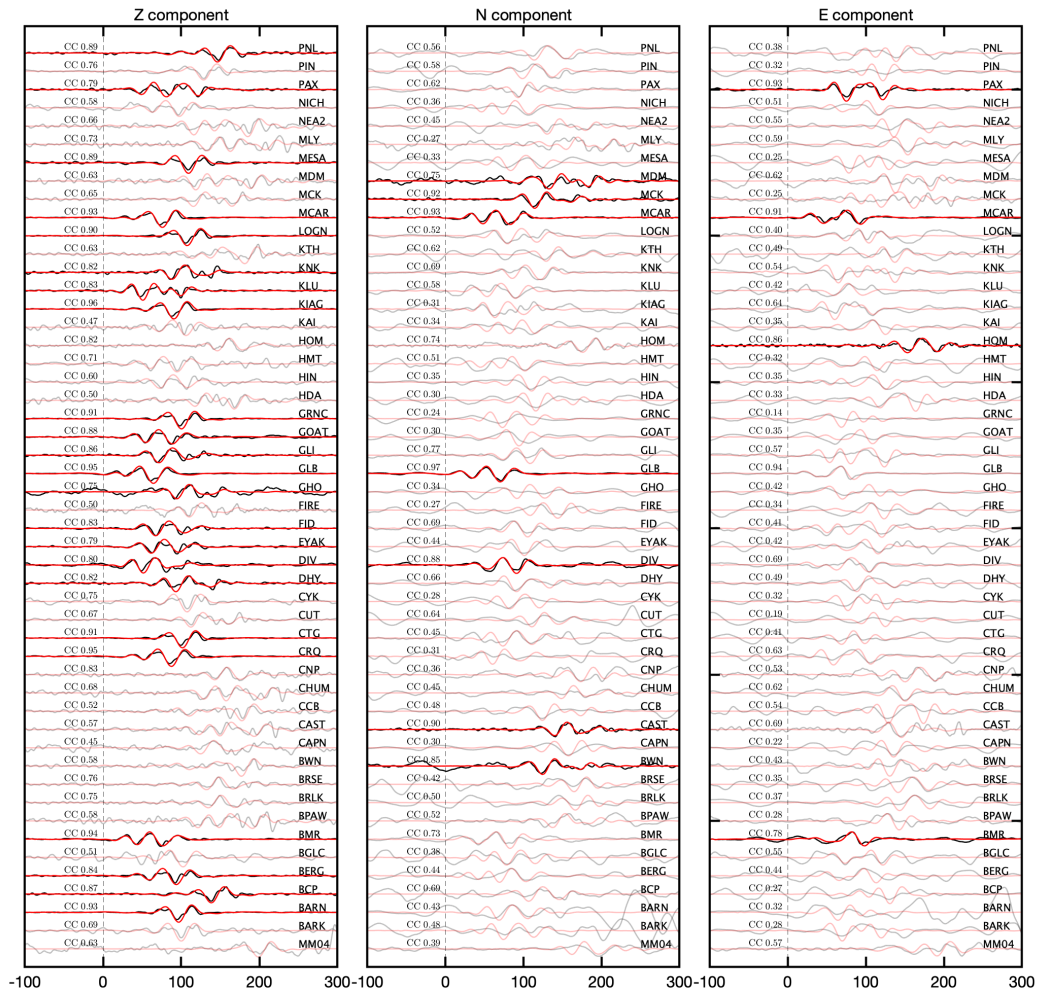
Figure S2. Observed and synthetic seismograms of the September 22, 2017 Wrangell Mountains landslide landslide for 50 stations within five-degree epicentral distance. Legends are similar to those Figure S1.
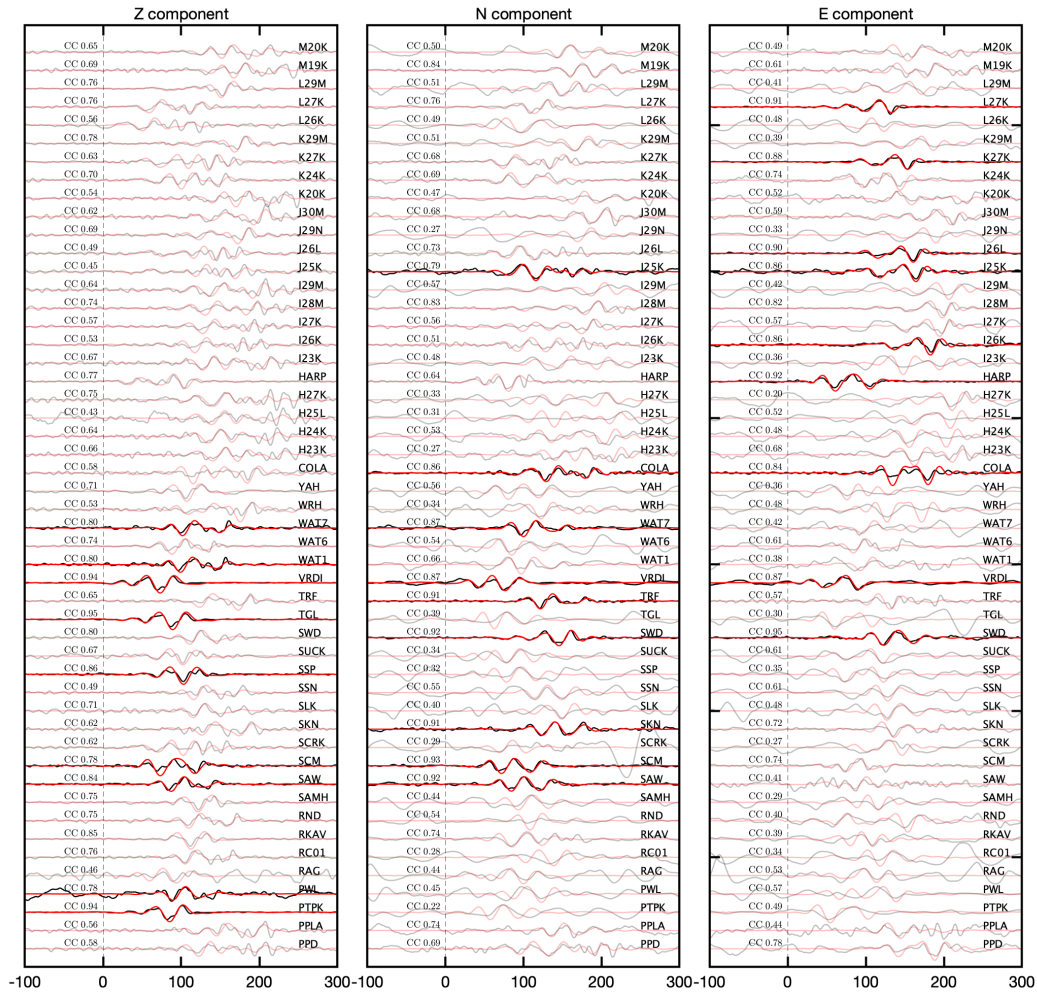
Figure S3. continued from S2. Observed and synthetic seismograms of the September 22, 2017 Wrangell Mountains landslide landslide for another 50 stations within five-degree epicentral distance. Legends are similar to those Figure S1.
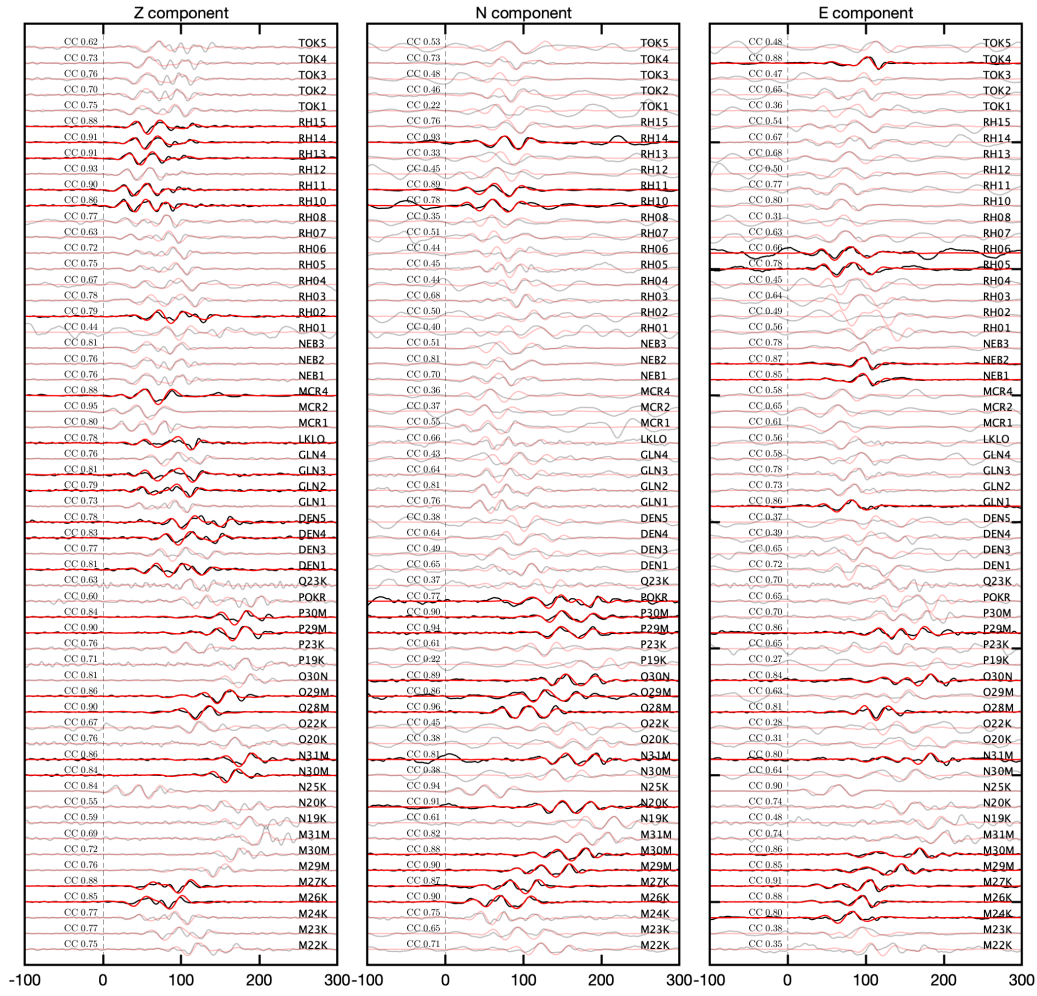
Figure S4. continued from S3. Observed and synthetic seismograms of the September 22, 2017 Wrangell Mountains landslide landslide for the remaining stations within five-degree epicentral distance. Legends are similar to those Figure S1.
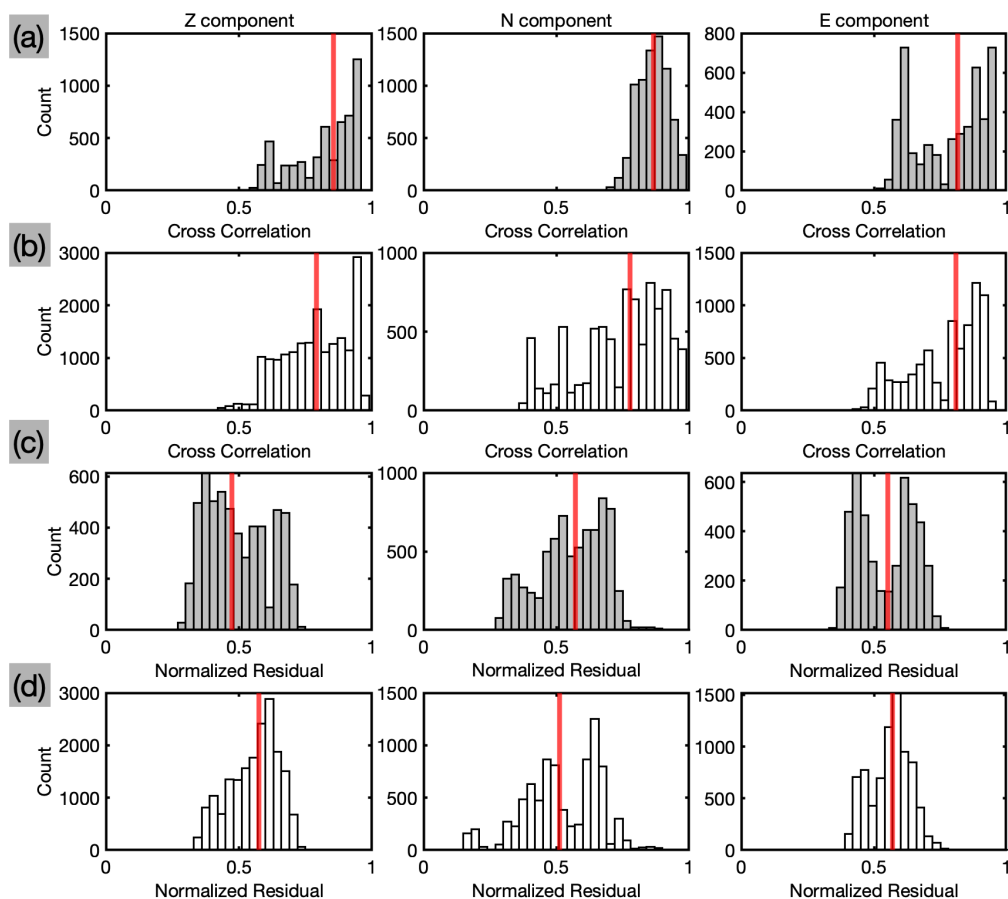
Figure S5. Histograms of the waveform residuals and cross-correlation coefficients from bootstrap realizations. (a) and (b), three-component cross-correlation coefficients of the observed and synthetic traces for the 2016 Lamplugh Glacier landslide and the 2017 Wrangell Mountains landslide, respectively. (c) and (d), three-component waveform residuals between the observed and synthetic traces for the 2016 Lamplugh Glacier landslide and the 2017 Wrangell Mountains landslide, respectively. Red lines denote the median values for each distribution.
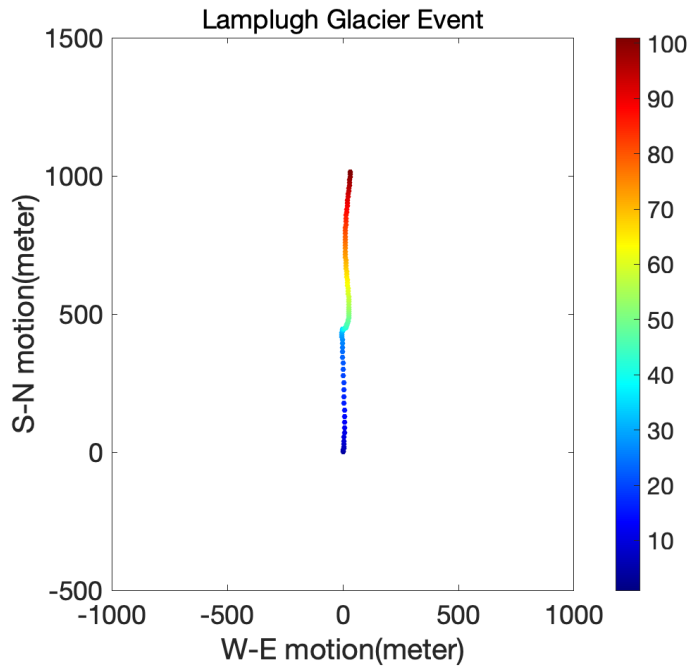
Figure S6. Horizontal displacement of the 2016 Lamplugh Glacier landslide. The mass used to calculate the displacement is 3.6×10^{11} kg (Toney & Allstadt, 2021)
.
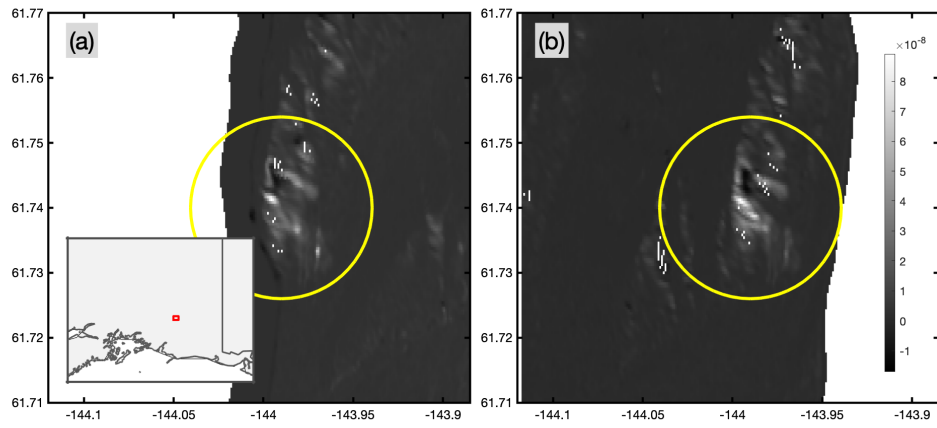
Figure S7. Differential radar amplitude calculated using two Sentinel-1 SAR images acquired before and after the 2017 Wrangell Mountains event. The yellow circles outline areas with enhanced backscatter that do not correlate with the local topography. (a), Differential amplitude of sub swath 2 (b), Differential amplitude of subswath 3.
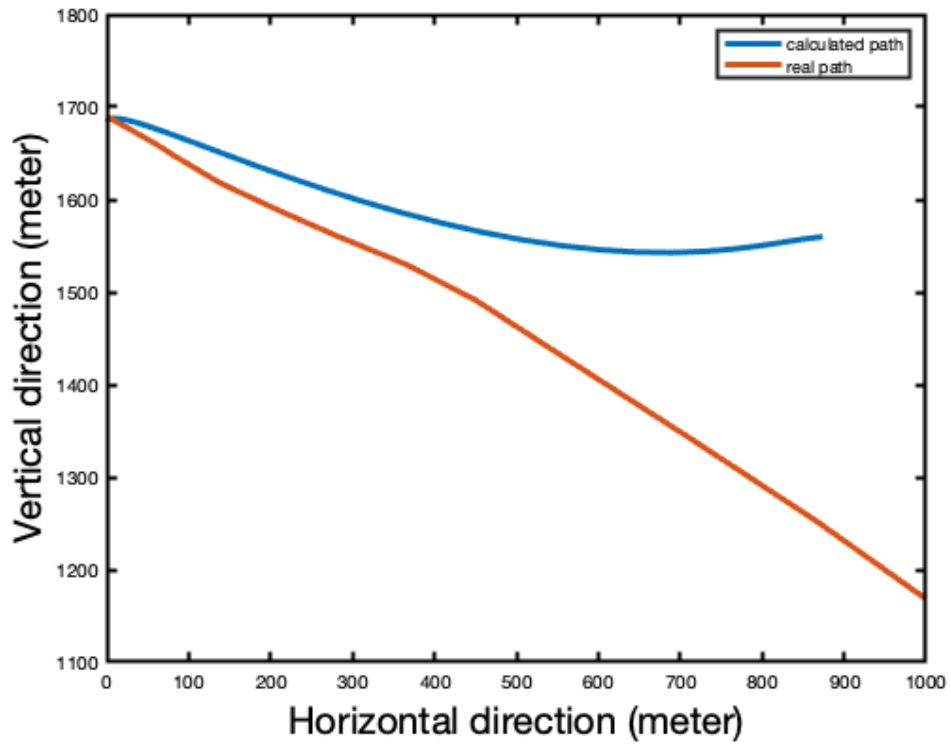
Figure S8. Vertical displacement of subevent 1 of the Wrangell Mountains landslide. Blue line is the vertical displacement integrated from the vertical acceleration. Red line is the measured elevation variation.
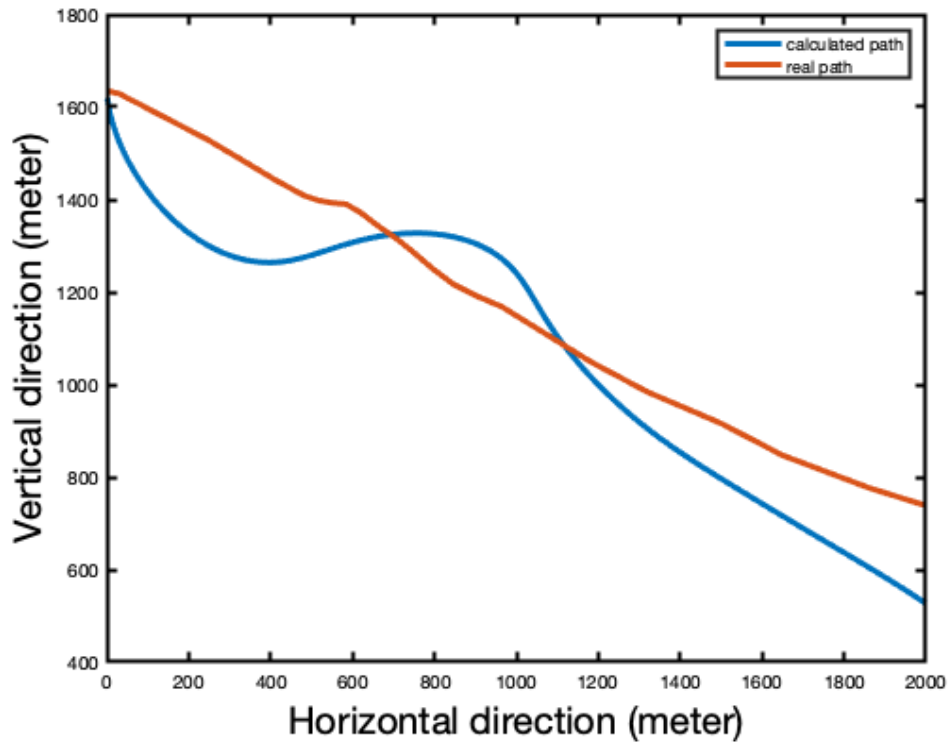
Figure S9. Vertical displacement of subevent 2 of the Wrangell Mountains landslide. Legends are similar to those of Figure S8.
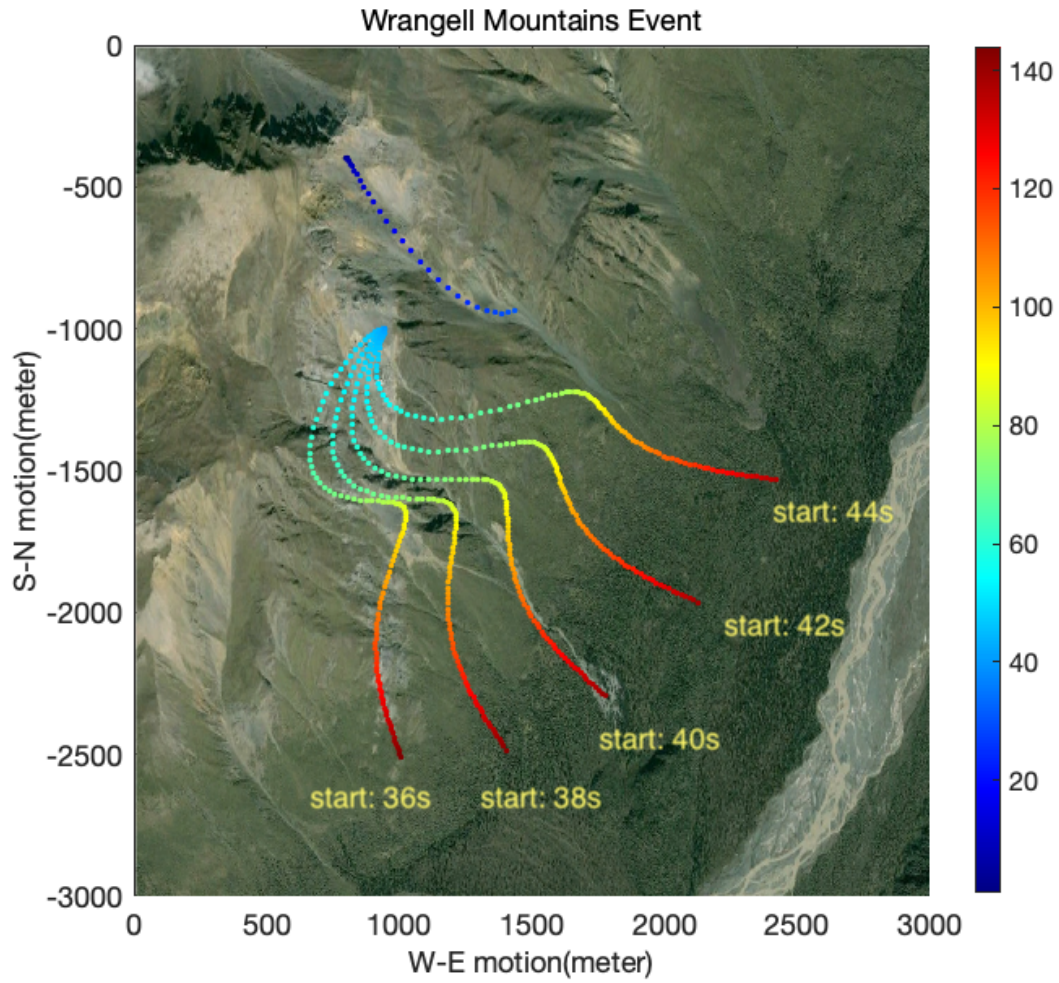
Figure S10. Horizontal trajectories determined from integrating the accelerations, assuming a mass of 1.5×10^9 kg for subevent 1 and a mass of 3.5×10^9 kg for subevent 2. Color dots represent the sliding time since the origin time. Background satellite image is from Google Earth provided by Maxar Technologies.
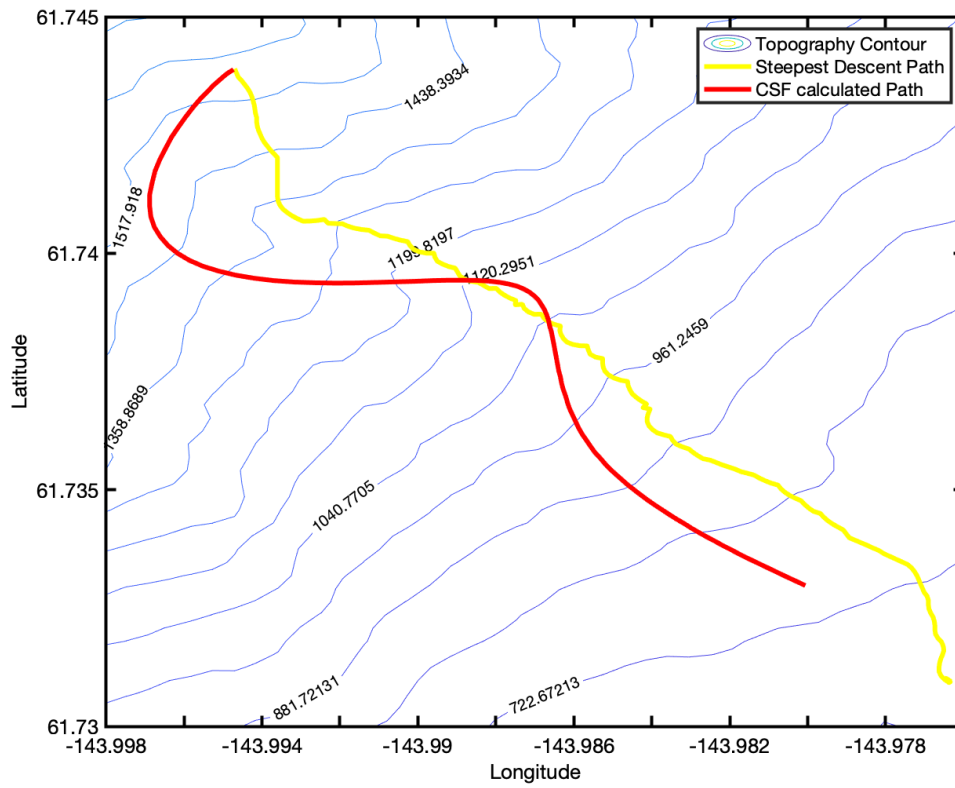
Figure S11. Horizontal trajectory of subevent 2 determined from using the preferred CSF model and the steepest descent path according to the ALOS AD3D30 digital elevation model.

References

Crowley, J., Hubbard, B., & Mars, J. (2003). Analysis of potential debris flow source areas on mount shasta, california, by using airborne and satellite remote sensing data. *Remote Sensing of Environment*, *87*(2-3), 345–358.

Ekström, G., & Stark, C. P. (2013). Simple scaling of catastrophic landslide dynamics. *Science*, *339*(6126), 1416–1419.

Gualtieri, L., & Ekström, G. (2018). Broad-band seismic analysis and modeling of the 2015 taan fjord, alaska landslide using instaseis. *Geophysical Journal International*, *213*(3), 1912–1923.

Toney, L., & Allstadt, K. E. (2021). lsforce: A python-based single-force seismic inversion framework for massive landslides. *Seismological Society of America*, *92*(4), 2610–2626.